Low Coefficient of Thermal Expansion Composite Tooling Manufactured via Additive Manufacturing Technologies

by

Michael Maravola

Submitted in Partial Fulfillment of the Requirements

for the Degree of

Master of Science in Engineering

in the

Chemical Engineering Program

YOUNGSTOWN STATE UNIVERSITY

December, 2018

Low Coefficient of Thermal Expansion Composite Tooling Manufactured via Additive Manufacturing Technologies

Michael Maravola

I hereby release this thesis to the public. I understand that this thesis will be made available from the OhioLINK ETD Center and the Maag Library Circulation Desk for public access. I also authorize the University or other individuals to make copies of this thesis as needed for scholarly research.

Signature:

_____

Michael Maravola, Student Date

Approvals:

_____

Dr. Pedro Cortes, Thesis Advisor Date

_____

Dr. Brett Conner, Committee Member Date

_____

Dr. Jason Walker, Committee member Date

_____

Dr. Salvatore A. Sanders, Dean of Graduate Studies Date

Abstract

The incorporation of additive manufacturing (AM) enables the ability to fabricate composite tooling molds rapidly and in a cost effective manner. This work has demonstrated the practice of an additive technology for manufacturing composite processing tools. In particular, this work has addressed tooling that is functional in the range of autoclave temperatures around 180°C. This has led to the use of Invar and ceramic materials for use in composite molding tools because of their relatively low coefficient of thermal expansion (CTE) performance, which is in range to that commonly displayed by carbon fiber reinforced composites during their solidifying curing process. In this project, three main approaches have been considered. The first innovative approach was based on printing a mold based on silica sand and infiltrating it with a polymer to yield a robust ceramic composite tooling. The second approach investigated the use of binder jetting to 3D print sand molds to cast molten Invar to produce the composite tooling. Indeed, 3D sand printing offers the ability to cast complex geometries without the geometric limitations associated with conventional pattern making. An additional technology using a Hybrid Direct Energy Deposition (DED) System for cladding Invar upon a steel molding structure has also been considered for producing potential composite tooling. Indeed, this unique approach could represent a promising technology for producing low cost composite tooling since only a small layer of Invar would be cladded to a non-expensive substrate. The results have shown that the aforementioned processes have successfully resulted on low CTE composite tooling molds. This work presents innovative AM processes by initially investigating additive manufacturing processes for composite tooling.

Acknowledgments

I would first like to thank my research advisor Dr. Pedro Cortes and my thesis committee members Dr. Brett Conner and Dr. Jason Walker. If it would not have been for Dr. Cortes' guidance, I would not be where I am at today. Thank you.

I would like to thank Brian Hetzel and Fireline Inc. for their guidance throughout this work and offering professional insight that otherwise may have been overlooked.

I would like to thank Steve Szaruga and the University of Dayton Research Institute (UDRI) for their guidance and assistance throughout this work.

I would like to thank my fellow graduate students for all of the good times we shared throughout my time here and whom I have made countless memories with.

Lastly, I would like to thank my friend and family for their devoted love and support, thank you all.

Table of Contents

List of Figures

List of Tables

1. Introduction

A composite is a system consisting of two or more constituent materials having different chemical or physical properties that when combined yield a system that exhibits the properties of their individual constituents. As materials become more advanced and commercially available, new manufacturing processes need to be developed for producing practical and applicable parts from these materials. According to a report published by Research and Markets, the composite tooling industry is projected to reach $551.8 Million (US) by 2021 while having a compound annual growth rate of 7.35% between 2016 and 2021 [1]. This projection suggests that as materials and manufacturing processes become more sophisticated, they will continue to be widely adopted by various industries. The annual global demand for carbon fiber composites is approximately 75,000 metric tons; of which the aerospace industry alone demands approximately 20,000 metric tons (26.7%) of the global demand of carbon fiber composites [2]. The aerospace and defense sector often take advantage of these composite systems as they typically offer impressive properties such as low densities, high mechanical strengths and low coefficient of thermal expansion [3]. Maintaining control over the mechanical and physical properties of composite materials throughout their fabrication process is a critical aspect to produce a high quality and dimensionally accurate part [4,5]. Indeed, the production of thermoset composites commonly require a tool for forming the parts. Composite tooling molds can be fabricated out of virtually any material; from cheaper materials such as fiberglass and plastics to expensive materials such as ceramics and iron-nickel super-alloys [6,7]. The limitations of the tooling materials arise as the specifications of the composite part increase, such as the

cure temperature of the resin and the dimensional stability. A common composite tooling practice is to use aluminum or steel as the tooling mold material (see Figure 1.1 on page 2).

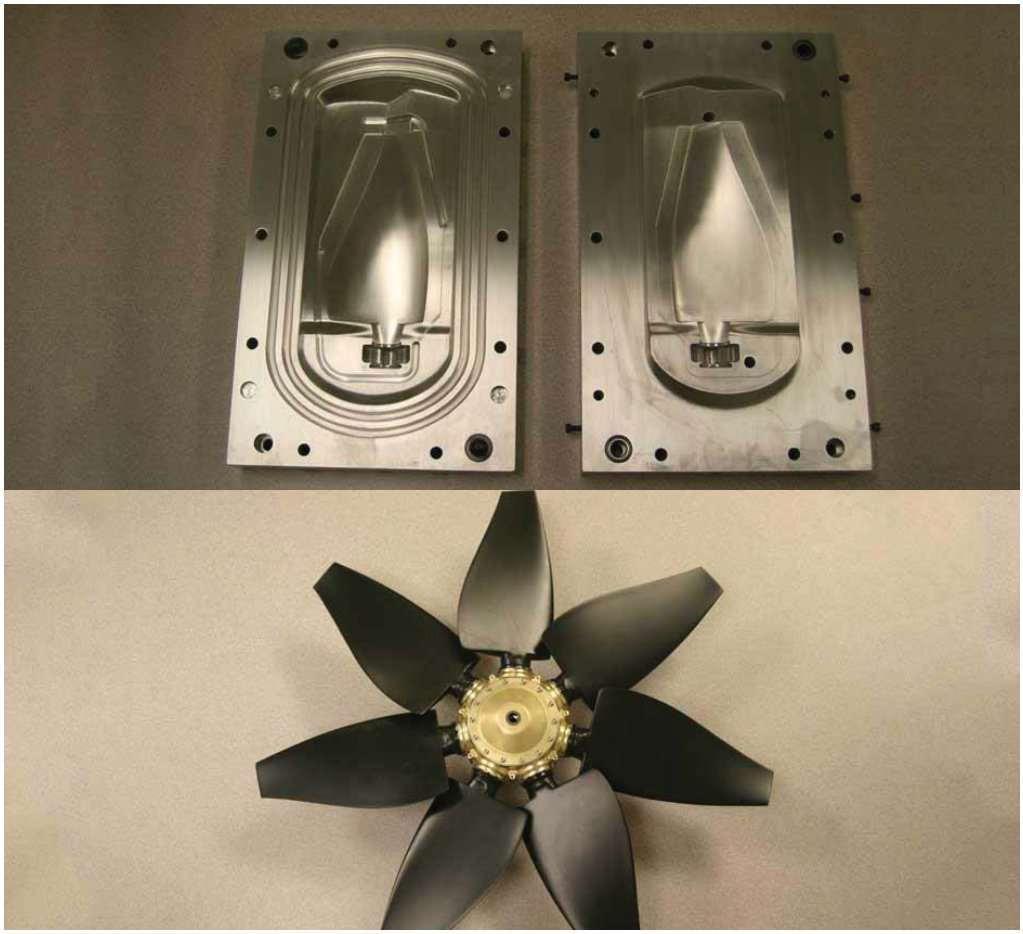

Figure 1.1: Aluminum tooling mold for producing rotary blades (above) and the resulting assembled part (below) [8].

Indeed, aluminum is commonly used due to its lightweight features and ease of machining. However, traditional aluminum tooling molds can have a lead time of 3 or more months and cost anywhere from a ~$10k to over $1M [9,10].

Additionally, composites produced with these tools may display significant geometric deformations due to the tool/ composite part interactions [11]. As composites are heated to achieve a final cure, typically around 175°C, the composite and tooling mold expand and contract at different rates [12]. For some applications, the geometric deformation that results from the difference in CTE can be neglected; however for aerospace applications it can be detrimental [13]. To avoid this phenomenon, low CTE materials such as ceramics and Invar-36 are used to produce the tooling mold. Indeed, due to the costs associated to the traditional manufacturing process of these materials, they are mainly used when low volume/geometrically complex parts are required [14].

Here, the use of additive manufacturing appears to offer a feasible alternative for producing composite tooling molds with significantly shorter lead times and/or lower production costs. [15]. The direct freeform fabrication of intricate geometric parts from specialty metals and ceramics that were difficult to process through traditional manufacturing methods is now possible via AM [16,17]. Mueller and Kochan discuss early implications of additive manufacturing in pattern making, and the effect of AM has on the traditional manufacturing process for producing sand molds within a foundry [18]. The process Muller and Kochan used, now referred to as binder jetting (see Figure 1.2) has significantly progressed as more materials are capable of being printed via this 3D printing process [19,20].

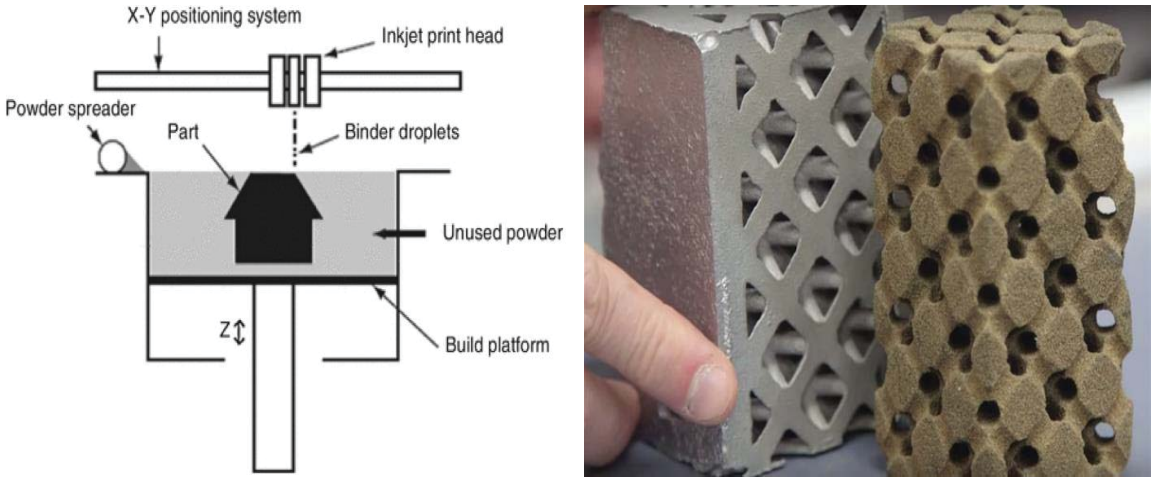

Figure 1.2 Binder jetting process (left) and a produced sand mold from a binder jetting process along with the casted part (right) [21].

Along with binder jetting which can print metal and ceramic parts, other modern AM processes such as selective laser melting (SLM) and direct energy deposition (DED) are capable of rapidly producing parts from titanium and titanium alloys, various steel grades, aluminum, Inconel, and Invar [22-24]. Though there are concerns of the total cost of ownership (TCO) for some of these AM processes, (lead time, energy requirements, technicians, and operating materials), it is expected the maturation of this technology will drive the costs down. Thus, an economic assessment will drive the adoption of these AM processes into larger, higher volume industries [25]. Table 1.1 compares commonly evaluated factors between AM and conventional manufacturing.

Table 1.1: Comparison of factors favoring AM versus conventional manufacturing [25]

AM Advantages	Conventional Manufacturing Advantages
Low production volumes	Large production volumes
Less material consumption	Easily processed/machined materials
High machining cost	Centralized manufacturing
Capital investment	
Logistics costs	
Transportation costs	
Prototyping	

From Frazier's review, the only economic shortcomings for metal AM are large production volumes, easily post processed parts, and centralized manufacturing facilities [25]. However, the benefits of metal AM, far exceed the shortcomings since low volume orders with high material and machining costs are detrimental to the product flow through a machining facility. In addition to the economic considerations, the incorporation of AM allows for almost limitless geometries of advanced materials which previously would have been very expensive to assemble or very challenging to produce [26-27]. Stratasys stands

out as a company that has made strides on producing compositing tooling molds via additive manufacturing as shown in the case study provided in Figure 1.3.

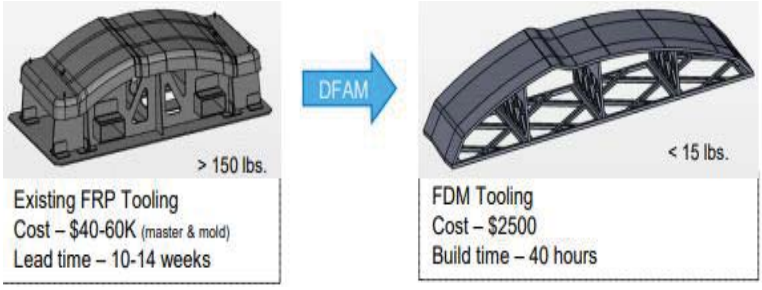

Figure 1.3: Economic case study of a traditionally manufactured composite tooling mold (left) and an additively manufactured composite tooling mold (right) [28]

Stratasys performed an economic case study comparing their 3D printed tooling mold to a traditionally manufactured tooling, which boasted an astonishing 90% decrease in cost and lead time by producing the exact same mold additively rather than traditionally [28]. Case studies such as these provide the motivation for continued research efforts towards developing new processes and material systems to achieve similar cost and lead time reductions. Hence the present research program has investigated the feasibility of producing low coefficient of thermal expansion composite structures to be used as tooling molds through different additive manufacturing processes.

Objective

The main objective of this work is to investigate different additive manufacturing technologies for producing low coefficient of thermal expansion composite tooling mold. Here, ceramic material systems and Invar-36 are investigated as the tooling material due to their low coefficient of thermal expansion.

Specific Objectives:

- Production of an Invar lead edge tool using a casting process based on a binder jetted silica sand mold.
- Manufacturing of an epoxy infiltrated 3D printed ceramic structure to be used as a tooling mold.
- Production of a tooling mold via binder jetting.
- Cladding of Invar-36 to a 316L stainless steel substrate via direct energy deposition.
- Thermal and mechanical testing of the material systems investigated
- Material characterization through SEM, XRD and EDS analysis techniques.

Organization

- Chapter 1 presents the motivation for this research program.
- Chapter 2 provides a literature review of the material and processes investigated along with the traditional and additive techniques used in fabricating composite tooling molds.
- Chapter 3 describes the experimental procedures used in the various manufacturing techniques investigate as well as the methodology applied on the, mechanical testing, thermal testing, and material characterization.
- Chapter 4 presents the results and discussion of the data collected.
- Chapter 5 summarizes and concludes the present work.

2. Literature Review

This chapter studies the materials and manufacturing methods used in producing composite tooling molds, both additively and traditionally. This review further explores each of the seven categories of additive manufacturing with a deeper focus on direct energy deposition and binder jetting since these two methods were the main technologies used in this work.

2.1. Materials Incorporated in Composite Tooling

2.1.1. Ceramics

Ceramics are inorganic materials that typically consist of at least two elements. Most ceramic materials are ionically bonded metal oxides such as magnesium oxide (MgO), silicon oxide (SiO_2), and aluminum oxide (Al_2O_3). The network formed between the positively charged cation and the negatively charged anion attributes the ensuing crystal structure of each material [29]. The strength of the ionic bond formed is determined by the difference in electronegativity between the two atoms with a larger difference yielding a stronger ionic bond. While most ceramics are ionically bonded, there are some exceptions where the materials are covalently bonded such as silicon carbide (SiC) or silicon nitride (Si_3N_4). Due to their bonding nature, ceramic materials often exhibit exceptional elastic moduli, low coefficient of thermal expansion, and good chemical resistance [30]. These properties allow ceramic materials to be used in many different industries as they can effectively withstand high temperature, and corrosive environments with a relatively long service life. Contrarily, due to their bonding nature, ceramic materials suffer from extremely brittle failure mechanisms as they exhibit virtually zero plastic deformation, which limits their application range. Additionally, advanced ceramics are traditionally

difficult to manufacture based on complex geometries. The following subsections will explore in more detail the properties of a few selected ceramic materials and their applications within the composite tooling industry.

2.1.1.1. Silica

Fused silica (SiO_2) more popularly known as quartz or fused quartz is the glassy, amorphous form of silica as it does not have a defined crystal structure. Fused silica differs from other glasses in such a way that it is essentially a pure substance, whereas other glasses contain impurities or other components [31]. As a result of its purity, fused silica exhibits thermal properties capable of withstanding high service temperatures and a very low coefficient of thermal expansion (0.54 $\mu m\ m^{-1}\ K^{-1}$ in the 0-800°C range) [32]. Fused silica is most commonly used in refractories due to its low CTE and thermal shock resistance, capable of being superheated and immediately quenched repeatedly. While the CTE is rather consistent across different sintering profiles, mechanical properties are affected by the degree of sintering due to a change in density. Wei Wan reported that sintering fused silica at 1275°C for 12 hours without a thermal shock at 600°C, yielded a high flexural strength (81.32 MPa) [32]. Thermal shock is when a rapid increase or decrease in temperature causes parts of a material to expand or contract at different rates. Thus, the resulting phase distribution of a fused silica part is effected by whether or not the part is subjected to a thermal shock while cooling after it has been sintered. In composite tooling, fused silica is typically used as the reinforcement component to an epoxy matrix system, often giving the resulting composite system greater mechanical strengths and better thermal properties than the epoxy alone. Hyu Sang Jo and Gyo Woo Lee conducted a study

where they showed that by increasing the weight fraction of fused silica in a composite system, the Young's modulus increased while the overall CTE of the composite decreased [33]. With the acclamation of 3D printing, more innovative methods of incorporating fused silica sands and powders into composite tooling are being sought after. One approach is 3D printing the composite tooling mold based on silica for further casting [34]. This process provides many advantages over traditional castings as it can increase the cooling efficiency of the sand mold with more intricate internal designs [35].

Silica also exists as crystalline silica (SiO_2), and is a material that has multiple crystalline phases (polymorphs) each having a tetrahedral crystal structure in which four oxygen atoms surround a central oxygen atom (Figure 2.1).

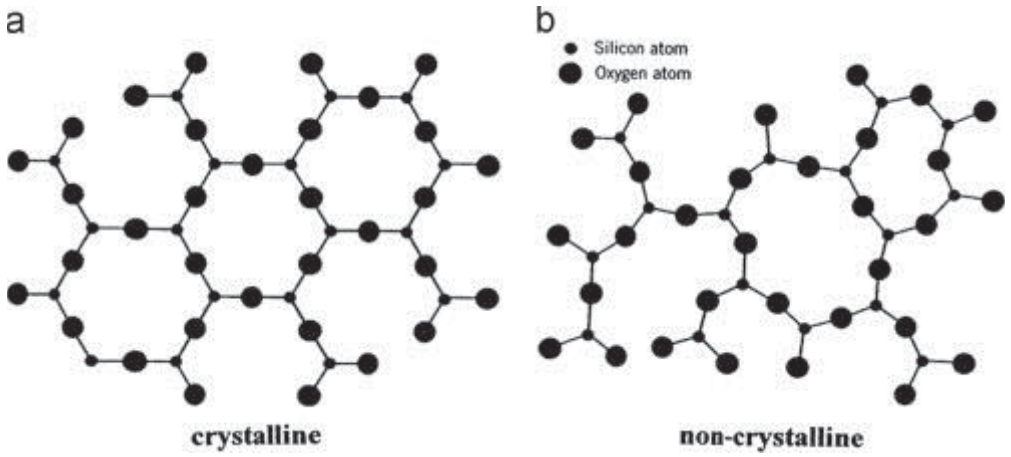

Figure 2.1: Structure comparison of crystalline silica (left) and amorphous fused silica (right) [36]

Figure 2.1 shows the symmetry of the crystalline silica over the non-crystalline silica, though bonded similarly displays no symmetry or order in bonding. With each phase

having the same tetrahedral structure, the differentiating factor is the number of vertices shared within the lattice, the bond length between silicon and oxygen, and the symmetry [37]. Swamy, V. et al intricately described the different crystalline phases that silica undergoes upon heating and cooling [38]. The most common phases of crystalline silica are alpha quartz, beta quartz, and cristobalite. Figure 2.2 depicts a pressure versus temperature equilibrium phase diagram for silica.

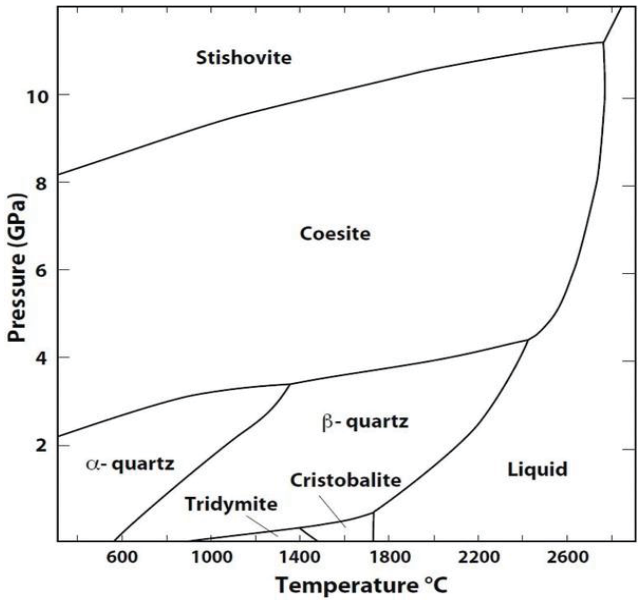

Figure 2.2: Pressure versus temperature phase diagram for silica [39]

According to Figure 2.2, when silica is heated under ambient pressure it will undergo two phase transformations: alpha quartz to beta quartz and then beta quartz to cristobalite. This is the typical phase transition path encountered upon sintering. The knowledge of the phase distribution within the resulting silica system after sintering is an important aspect, since certain phases are capable of compromising final system properties. Here, the formation of cristobalite yields good chemical resistivity systems however it sacrifices the mechanical

properties [40]. For instance, Breneman and Halloran showed that the amorphous fused silica retained about the same strength at temperatures of 25°C and 350°C whereas the crystalline silica having a larger phase distribution of cristobalite exhibited greater strengths as 350°C than 25°C [41].

2.1.1.2. Zirconia

Zirconia (ZrO_2) is the oxide form of zirconium. The three known phases of zirconia are monoclinic, tetragonal and cubic, each occurring as the temperature increases suggesting that the greater the temperature, the greater the symmetry [42]. Zirconia ceramics have many industrial applications due to its chemical resistivity, thermal (CTE of 10.0 $\mu m\ m^{-1}\ C^{-1}$), and mechanical properties (compressive and flexural strength of 2000MPa and 1300MPa respectively) [43]. Zirconia is commonly used as a filler or component in other systems to develop composite systems capable of applications in the biomedical field and other industries [44-46]. Zirconia is commonly alloyed with stabilizing metal oxides (CaO, MgO, Y_2O_3) to retain its tetragonal structure at room temperature. The prevention of the phase transformation from tetragonal to monoclinic allows the modified zirconia system to be more efficiently inhibit crack propagation. Thus, zirconia is often used to strengthen mullite ($3Al_2O_32SiO_2$ or $2Al_2O_3SiO_2$ depending on the oxidation number of the aluminum) to form mullite-zirconia composites [47]. Rendtorff et al has shown that by introducing zirconia into the mullite mixture, the fracture toughness of the composite system increases (from ~1.7 $MPa{\cdot}m^{1/2}$ at 15 wt.% zirconia to ~2.5$MPa{\cdot}m^{1/2}$ at 85 wt.% zirconia) [48].

2.1.2. Metals

Metals are another class of materials that can exist as pure elements, compounds, or alloys. They are often very hard in their solid state and shiny in appearance (provided the surface is not oxidized or tarnished). Metals are ductile and malleable with good electrical and thermal conductivities, making them very workable and practical for a wide range of applications. The good electrical and thermal conductance is a result of the consistent emission of outer shell electrons from the metallic atoms, resulting in a global delocalization of electrons around and throughout the system.

2.1.2.1. Invar

Invar 36, is an iron-nickel alloy containing 36% nickel, which is particularly known for its low coefficient of thermal expansion (~3.6 μm/m°C) up to around 200°C [49]. Peculiarly, this phenomenon is observed only around a composition of 36% nickel. This impressively low thermal expansion, also known as the "Invar effect" is explained via two physical mechanisms of invar; the normal lattice expansion and the anomalous contraction [50]. These separate phenomena were first pointed out by G. K. White in which he explained the temperature dependencies on the specific heat of invar for the normal lattice expansion and how such dependencies follow the Grüneisen relation [51,52]. The Grüneisen relation, formulated by the German physicist Eduard Grüneisen describes the effect that the volume changes of a crystal lattice is a function of the material's vibrational properties and in turn the way the material dynamically functions at different temperatures [53]. Through the theoretical application of models and hypotheses, Rancourt et al has shown that the Invar effect depends on the energetic state of the Fe-Fe bonds and the number of unsatisfied

energetic Fe moments which results in the magnetically "frustrated" Invar system [54]. This "frustrated" magnetic system opposes the thermal expansion of the alloy until the Curie temperature is reached (230°C), at which point, the material becomes paramagnetic and proceeds with a relatively normal thermal expansion as the temperature continues to increase.

Due to its thermal properties, Invar-36 is an ideal material for composite tooling molds. It has an austenitic crystal structure, and is capable of resisting the cyclic stresses induced from repeated autoclave curing cycles giving it an exceptionally long tooling life [55,56]. Quite often in the aerospace industry, carbon fiber reinforced epoxy (CF/Epoxy) systems are the composites of choice having an effective CTE of about 2.9 to 3.66 μm/m°C making Invar-36 an ideal material for a composite tooling mold due to the similarity in the CTE [57]. However, it is important to note that Invar is very expensive to machine traditionally, and is relatively dense compared to other composite tooling mold materials such as aluminum.

2.2. Manufacturing Methods

2.2.1. Traditional Manufacturing Methods

A manufacturing industry is defined as any business or entity that uses components, parts, or raw materials to produce a finished good. Manufacturing has evolved throughout history from the skilled hand work of artisans to the mass production following the industrial revolution. Almost every material has multiple manufacturing methods, with the ideal

method often being dependent on the application. The following sections explore the common manufacturing processes for both metals and ceramics.

2.2.1.1. Metals

The three main manufacturing processes for metals are: A) casting, B) forming, and C) subtraction. The process used depends on the material and the application requirements. Some metals are simply melted down and cast directly into their near net final dimensions.

A) Casting is a high temperature process that operates above the metals melting temperature (T_m) to allow the metal to flow into a mold. The molds themselves need to be durable and able to withstand the thermal shock of the molten metal. Limitations of this process arise in the fabrication of the mold [58]. Indeed, since molds are almost always ceramic based materials, producing complex geometries is a challenging task [59].

B) Forming processes are manufacturing techniques where metals are deformed in a desired shape without further addition or subtraction of materials. Common forming processes include: a) rolling, b) pulling, c) extrusion, and d) forging; all of which can be performed in either hot or cold environments depending on the properties and phase distribution desired on the final product [60,61]. A brief description of each process is here presented:

- Rolling techniques take cast slabs of metal and compress them, giving a uniform thickness. Some common products from rolling are: sheet metals, rail road track, I-Beams, and guardrails.

- Pulling (drawing) processes stretch the material out of a die via an applied tensile stress. Sheet metal, bars, tubes, and wires are all applicable forms that undergo the drawing process. Regardless of the metal form, the applied tensile stress is limited by the tensile stress of the material being pulled.
- Extrusion is similar to pulling except that in extrusion forming, the metal is subjected to compressive forces rather than tensile. Advantages of extrusion process are the ability to create complex cross sections and internal cavities within the final product.
- Similar to extrusion, forging techniques apply a compressive force upon the metal, however these compressive forces are localized. Forging process have existed since metalworking was invented thousands of years ago as it was the traditional method of metalworking for blacksmiths. Industrial forging is carried out using large presses and hammers to compress the manufactured. Final metal products from forging process are often stronger than that of casting or machined process because of the resulting grain structures induced from shaping the part [62,63].

C) Subtractive manufacturing and machining is a process consisting of the removal of material from a part to produce a final structure. Subtractive manufacturing often starts with a raw block of material and mills or cuts away material, (similar to sculpting a statue) until the final net shape is achieved. Modern subtractive manufacturing and machining processes are performed on a computer numerical control (CNC) machine. Machining paths and tool changes can be programmed into a CNC machine allowing it to automatically remove material from the part. This significantly reduces labor cost as

technicians are generally only required for the setup and tear down of the job. There are many forms of subtractive manufacturing and machining techniques, Table 2.1 provides a summary of various subtractive methods for metals.

Table 2.1 : List of commonly practiced industrial subtractive machining methods [64]

Process	Description
Turning	Method used to create rotational parts by either rotating against a fixture or fixed and pressed against a lathe or cutting tool
Drilling	Creating a new, round hole within a part
Boring	Enlarging a previously existing hole within a part
Reaming	Finishing the edges of a previously drilled or reamed hole
Milling	Feeding a rotating cutting edge against a part at different directions to obtain a final net shape
Sawing	Utilizing an oscillating or rotating blade to cut a part
Broaching	A toothed tool used to machine internal passage ways within a part
Planing	Single point cutting against a part to sculpt or plane the surface
Grinding	Method of abrasively removing material from a part to either knock down sharp edges or to achieve a desired surface finish

2.2.1.2. Ceramics

As with metals, there are three main manufacturing methods for ceramic materials; they are: A) casting, B) pressing and C) extruding. The ceramic manufacturing processes are parallel to the metal manufacturing processes.

A) Casting ceramic materials is similar to the casting process of metals except that the ceramic is not heated to its T_m. Ceramic powders are usually suspended in water and poured into the mold. This liquid is referred to as the slip, and once in the mold, the water is then evaporated from the slip leaving just the ceramic material. From here, the mold containing the ceramic powder is fired in either in a kiln or a furnace to sinter the solid part. Figure 2.3 shows a process diagram for a traditional slip casting process.

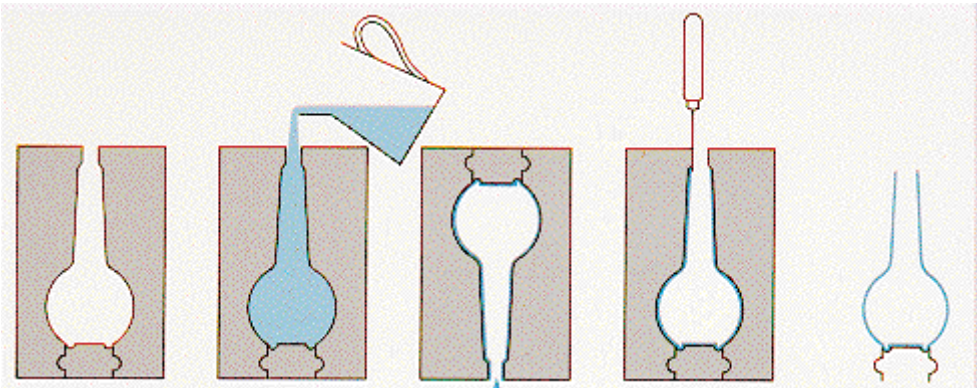

Figure 2.3 : Schematic of a traditional slip casting process [65]

B) The ceramic pressing process is similar to casting with the difference being that the ceramic can be either wet or dry. Here the ceramic is allowed to fill a mold. Once filled, a die presses the material to shape where the resultant part is then in its green state. Additional post processing can be performed on the green state parts to achieve greater

densities or mechanical properties upon sintering. The additional post processing steps are cold isostatic pressing (CIP) and hot isostatic pressing (HIP). CIPing is carried out at room temperature and requires sintering afterwards; whereas HIPing is performed at high enough temperatures that post-secondary sintering is not required [66].

C) Extruding ceramics is analogous to the extrusion process of metals. A ceramic slurry is compressed through a die, retaining the dimensions of the die. Bricks are typically manufactured in this manner due to the high volume output of the die extrusion systems. If a chamber is added on the other side of the nozzle where the slurry is compressed, then it becomes an injection mold process. Using injection molding techniques for ceramics allows for the fabrication of more complex geometries or precision parts.

2.2.2. Additive Manufacturing Methods

This section describes the seven recognized categories of additive manufacturing (AM) [67]. Indeed, there are other techniques of AM however they all stem from one the following methods. All methods of additive manufacturing fabricate 3D parts in accordance to a preprogrammed computer aided design (CAD) drawing. Within each subsection, a brief process overview is provided along with the materials each process is capable of printing.

2.2.2.1. Vat Photopolymerization

Vat polymerization also known as stereolithography apparatus (SLA) was the first commercialized 3D printing process developed by 3D Systems in 1987 [68]. SLA is a method based on curing a liquid photopolymer with an ultraviolet (UV) light in a layer by layer fashion. The UV light initiates the cross-linking; within the photopolymer resin yielding a solid, isotropic part. As of now the list of printable materials in the SLA process is limited to mostly plastics because a photopolymer is required to initiate the crosslinking, however there are new ceramic/photopolymer resins being produced which could provide many practical applications [69,70].

2.2.2.2. Material Jetting

Material jetting (MJ) is a method that prints liquid photopolymer similarly to the SLA process except that in the MJ, the photopolymer is deposited by a print head. In the MJ process, drops are deposited either continuously or dropped on demand (DOD) in a layer by layer fashion. The materials used in MJ are mostly thermoset plastics and waxes that are photosensitive to a UV cure. Liquid photopolymers are used in continuous deposition printheads because they have a low viscosity. The DOD method is used for more viscous materials to create wax like parts that are typically used to manufacture investment casting molds [71]. One of the most innovative uses of MJ 3D printers is the ability to print multi-material and functionally graded parts, giving the final part regions of different mechanical, thermal, or electrical properties [72]. In addition to functionally graded materials, XJET just introduced a printable ink containing ceramic nanoparticles capable of being printed

at a layer thickness of 10 μm. Parts printed with this nanoparticle ink at layer thicknesses of 10 μm are reporting greater than 99% relative densities [73].

2.2.2.3. Material Extrusion

Material extrusion, more commonly known as fused deposition modeling (FDM) is the most widely adopted and cheapest method of AM. It was originally developed in the 1980s by Scott Crump, the future cofounder and chairman of Stratasys Ltd. FDM 3D printing extrudes a plastic filament through a nozzle at a continuous, constant rate. The nozzle and print bed are heated to allow the plastic filament to flow through the nozzle and stick to itself without lifting off the build plate. After a layer is printed, each sequential layer is then fused on top of one another until a solid 3D part is consolidated. The most common materials printed via FDM are polylactic acid (PLA) and acrylonitrile butadiene styrene (ABS); however many specialty materials are continuously being produced [74]. Some specialty FDM machines can print carbon fiber, onyx, nylon, and even continuous fiber materials [75,76]. Most of the builds performed via FDM are used for conveying or prototyping ideas rather than a direct application. FDM is the most commercialized AM technology with benchtop models obtainable for less than $1000 to industrial models costing anywhere from $10,000-$300,000 [77].

2.2.2.4. Powder Bed Fusion

The powder bed fusion (PBF) process is a method of AM that encompasses several AM techniques such as: selective laser sintering (SLS), selective laser melting (SLM), selective heat sintering (SHS), electron beam melting (EBM), direct metal laser sintering (DMLS),

and direct metal laser melting (DMLM). Generally, in the PBF processes there are two powder beds and a laser system that binds or fuses the material together in accordance to an uploaded CAD file. A roller or spreading mechanism spreads an even layer of powder across the build area. On average, the layer height is about 100 microns but can be decreased down to 20 microns to achieve a better surface resolution and denser part [78,79]. Once the powder is spread, the laser melts or sinters the thin layer of powder. The differentiating factor for these methods is either the energy source or the interaction phenomena when the energy is applied. For instance, EBM uses an electron beam as the energy source which requires the system to be under vacuum, whereas SHS uses a heated printhead to fuse thermoplastic powders together.

2.2.2.5. Sheet Lamination

Sheet lamination is a method of AM where sheets of material are layered on top of each other and adhered together in a specific fashion depending on the working material. Commonly referred as laminated object manufacturing (LOM), this process was commercialized in the early 90's [80]. The process consists of feeding the rolled material over a build platform, followed by a heated roller that applies a bonding adhesive to the sheet. After the adhesive is applied and another layer of material is applied, and then a CO_2 laser cuts the excess sheet material in the programmed pattern. The laser typically cross-hatches the material making it easy to remove from the final part after the build is finished. Another method of sheet lamination is ultrasonic additive manufacturing (UAM), where sheets of metal are adhered together via ultrasonic welding [81]. The post processing of this method is more complex since CNC machining is required to remove the excess metal.

2.2.2.6. Direct Energy Deposition

Direct energy deposition (DED) is a method of additive manufacturing that utilizes a heat or a power source to directly deposit metal onto a substrate to form a 3D geometry. The two primary methods of DED are wire feed and powder feed. Both systems contain heat sources most commonly consisting of a neodymium yttrium aluminum garnet (Nd-YAG) laser, a CO2 laser, or an electron beam. The wire or powder is fed through the system until it contacts the laser. There is usually a shield gas around the laser which protects the material being deposited and the build area from reacting with oxygen and moisture in the air. Shield gases are usually inert or semi-inert mixtures of gases with very low heat transfer coefficients and are typically denser than air to better insulate the weld. Argon is the most common shield gas; indeed, other gasses such as oxygen, carbon dioxide, helium, and hydrogen are used. However, these they are typically mixed with argon in some proportion. Without the shield gas, oxidation could occur and hinder the quality of the build [82]. Upon contacting the laser, the material is essentially welded into the desired parts. Critical parameters for this process include: laser power, feed rate, transvers speed, and spot size, all of which directly impact the quality of the build. Figure 2.4 contains a diagram of a traditional DED apparatus.

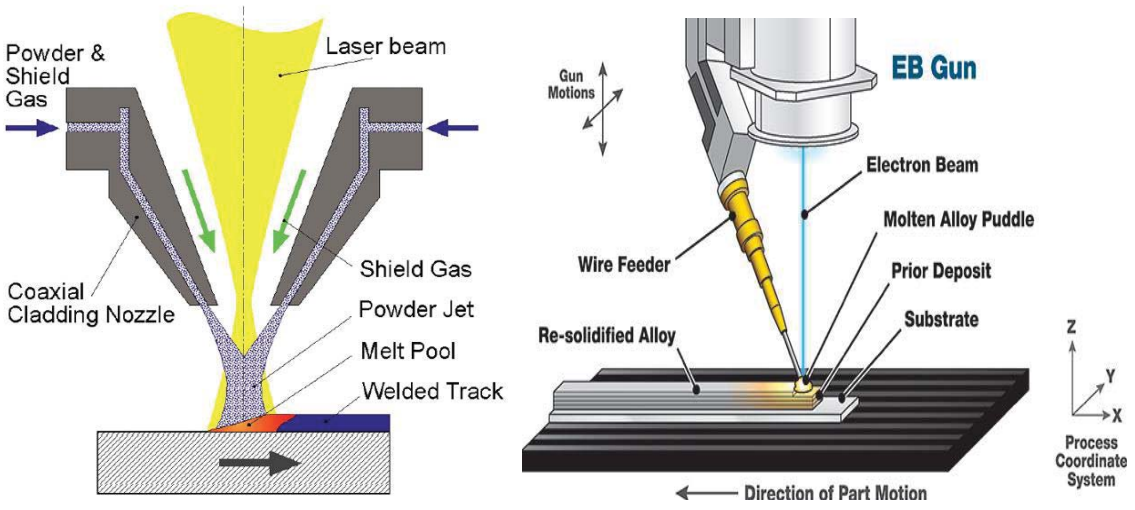

Figure 2.4 : Comparison of a DED powder process (left) and a wire feed process (right).

DED differs from SLM and DMLS because in DED, the wire or powder is fed directly, whereas in SLM and DMLS, the powder is spread out layer by layer. A main concern that arises from these AM techniques is the amount of residual stresses created from the large temperature gradients and phase transitions [83]. Additionally, the build direction can impact the mechanical quality of the part as studies have shown that dendritic growth is affected from the direction of the build [84]. This in conjunction with the temperature gradients can produce enough stresses and dislocations in the final part to compromise the mechanical integrity. This has resulted in the study and development of models to predict the internal residual stresses to determine the mechanical integrity of the part after the build. Many models have been developed using finite element analysis (FEA) over the past twenty years such as the Heigel, Michaleris, and Reutzel work; where they predicted the thermal stresses produced throughout the print with only an 11% error compared to the recorded in-situ stresses [85,86].

DED is of interest to the composite tooling industry due to the ability to develop functionally graded materials (FGM) with a predetermined CTE [87]. Bobbio et al demonstrated the ability to functionally grade Ti-6Al-4V to Invar 36 linearly via DED [88]. They modeled the above process and predicted all of the secondary phases formed (all of which were confirmed using alternative analysis techniques) that were suspected to lead to cracks formed in the final structure. The ability to fabricate FGM allows the manufacturer to build the bulk of the part out of a cheaper material and clad only the working surface with the more expensive material system.

2.2.2.7. Binder Jetting

Binder jetting is an additive manufacturing process in which a liquid binder is deposited onto a powder bed to build a 3D part. The powder is supplied either through a hopper system or a powder box and is spread via a roller system. The build plate is piston driven and incrementally lowers by a pre-established layer thickness after each layer is printed. The same method applies for powder box systems; however, instead of initially lowering, the build plate rises, allowing the roller to spread the powder across the buildbox. Figure 2.5 displays a schematic of a binder jetting process.

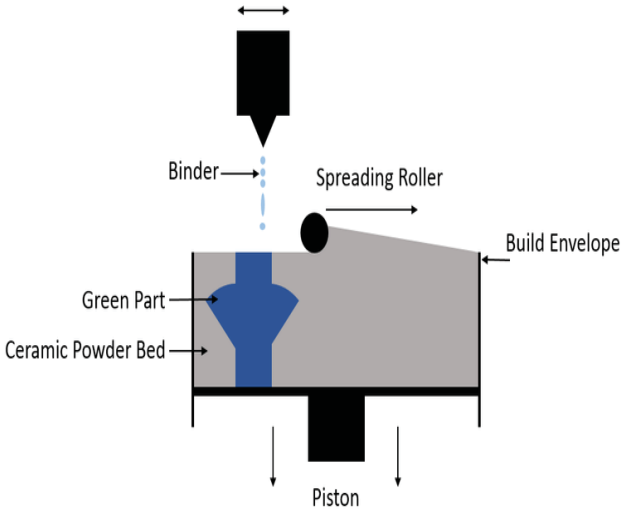

Figure 2.5: Binder jetting system depicting the powder spreading and binder deposition processes.

Here, the green part is observed immersed in the powdered bed while the roller spreads the next layer of powder. In binder jetting, the entire build envelope is filled with powder requiring the part be depowdered. Binder jetting requires several post processing steps to fully produce the part. For instance, once the part is removed from the build plate, the part is transferred to an oven to cure the binder. The curing temperatures at this stage are in the 60°C to 200°C depending on the binder specifications. After these steps, the part is in its "green state" and is solid enough to be handled, although it does not retain the mechanical properties of the fully cured parts. Studies and comparisons the mechanical properties of parts in their green state are often advantageous in determining how the process variables may affect the quality of the final sintered part [89]. Some printing process variables include: transverse velocity, layer thickness, binder to material ratio, binder saturation

percentage, choice of binder, build plate temperature, build direction, and steric orientation of part. The final curing process varies upon the specific printed material. Typically, both metals and ceramics are sintered to achieve a higher density and greater mechanical properties [90]. In addition to sintering, both ceramic and metal parts can further be processed with the infiltration of a metal to form metal matrix or ceramic matrix composites [91].

The binder jetting processes is particularly interesting to the composite tooling industry due to the capabilities of printing ceramics. Ceramics which have a near zero coefficient of thermal expansions are ideal for composite tooling molds as they will neither expand nor contract while the composite part is curing. Traditionally, the manufacturing process of intricate ceramic geometries for industrial purposes was nearly impossible. Thus with the incorporation of binder jetting, composite tooling patterns can effectively be manufactured out of ceramics, providing a cost effective alternative process.

2.3. Composites

Composites are defined as materials made from two or more constituent phases having different chemical or physical properties that when combined produce a single system with characteristics from the individual components [92]. Composite materials consist of a matrix material and a reinforcement phase. The matrix can be organic materials such as epoxies or other polymers or inorganic materials such as cements, metals, or ceramics. Similarly, the reinforcement phase can be organic or inorganic, and can have a wide range of geometric configurations (fiber, powder, particulate, etc). Fibers are the most common

however particle reinforcement is also used. There are three main classifications of composite materials: ceramic matrix composites (CMC), metal matrix composites (MMC), and polymer matrix composites (PMC). Each type of composite has a unique manufacturing process and individual platform of benefits which is discussed in more detail in the following sections.

2.3.1. Ceramic Matrix Composites

Ceramic matrix composites (CMCs) consist of fibers or powder embedded within a ceramic matrix. CMCs commonly exhibit low densities, good mechanical and thermal properties, and good corrosion resistances; even at high temperatures. [93]. Common reinforcements used within CMC's are carbon fibers/particulates, carbon nanotubes (CNTs), glass fibers, alumina fibers, and silicon carbide fibers/particulates. These materials are used to reinforce the existing ceramic matrix of alumina, silica, zirconia, or SiC to name a few. CMCs are commonly used for turbines and jet engines as they are about one third the weight of nickel based superalloys and can function at higher temperatures [94]. Zhu et al [95] developed a novel process to fabricate carbon fiber/SiC composites via SLS. They showed systems with a flexural strength of 249 +/- 17.0 MPa, with service capabilities at high temperatures (see Figure 2.6).

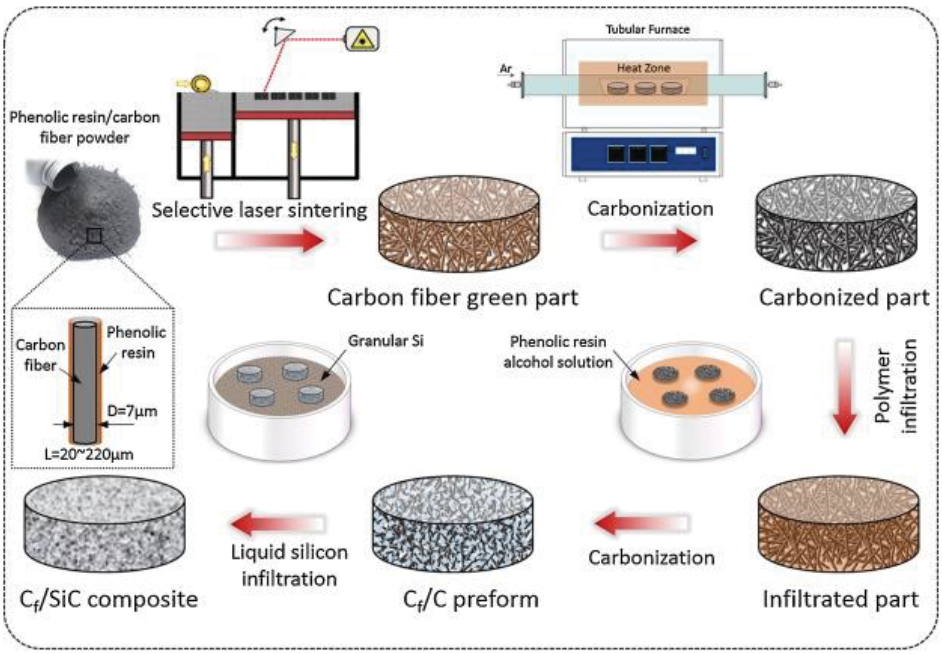

Figure 2.6: Manufacturing process for carbon fiber reinforced SiC parts produced via SLS 3D printing and infiltration of liquid silicon [95]

In addition to high temperature applications, CMCs find themselves widely used in prostheses and orthopedic applications due to their long term wear resistance and biocompatibility [96,97]. Alumina, zirconia, and alumina reinforced zirconia are the common composites investigated to form the socket for total hip replacements [98].

2.3.2. Polymer Matrix Composite

Polymer matrix composites (PMCs) generally are either thermoplastic or thermoset resins reinforced with a fiber network. PMCs are classified into two categories: reinforced plastics and advanced composites. Reinforced plastics are simply resins reinforced with low stiffness fibers. An example of this is polyester resin reinforced with glass fibers to make

fiberglass; which holds the largest market share in the PMC industry [99]. Advanced PMCs are similar except they exhibit significantly greater strengths than regular reinforced plastics. This is a result of the more expensive carbon and aramid fibers used as reinforcement in these systems. The fiber networks are either continuous (woven fabrics) or discontinuous (chopped), each having different properties [100]. Figure 2.7 shows a schematic comparison between continuous and discontinuous fibers. Common reinforced fibers used in PMCs are glass fibers, carbon fiber, and Kevlar (aramid) fibers. Continuous fiber reinforced composites exhibit high tensile strengths in the longitudinal direction relative to fiber orientation.

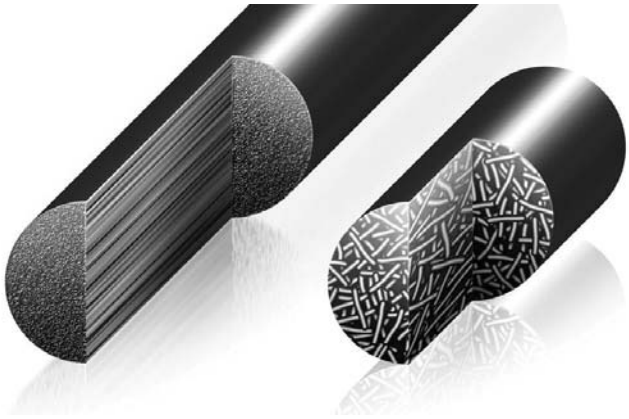

Figure 2.7: Graphic of continuous woven graphite fibers (left) and discontinuous graphite chopped fibers (right)

Nowadays, with Markforged's advances in FDM and filament preparation, it is now possible to print continuous fiber filament using PLA, ABS, or Nylon. Dickson et al [101] published their work demonstrating the benefits of 3D printing continuous carbon fiber, glass fiber, and Kevlar fiber composites displaying high flexural and tensile strengths (see

Table 2.2) [101]. One major drawback of PMCs is that the strength and stiffness are temperature sensitive which limits them from high temperature applications [102].

Table 2.2: Summary of mechanical data from 3D printed continuous fiber specimens labeled as 'A' for concentric and 'B; for isotropic respectively [101].

Specimen	Tensile Strength (Mpa)	St dev	Elongation at break (%)	St dev	Elastic Modulus (Gpa)	St dev
Nylon	61	1	439.00	2.55	0.53	0.02
CF_A	216	26	4.22	0.9	7.73	0.39
KF_A	150	10	4.23	0.8	3.61	0.54
KF_B	164	9	4.98	0.32	4.37	0.59
GF_A	194	1	8.97	0.43	3.12	0.15
GF_B	206	5	8.42	0.57	3.75	0.89

Specimen	Flexural modulus (GPa)	St dev	Flexural strength (MPa)	St dev	Flexural toughness (J/m^2)	St dev
Nylon	1.06	0.07	41.98	0.78	262.32	4.21
CF_A	13.02	1.04	250.23	14.61	356.51	28.00
GF_B	4.21	0.32	196.75	8.06	693.88	68.50
GF_A	3.87	0.07	165.79	5.79	650.90	29.19
KF_B	6.65	0.23	125.80	3.27	390.62	16.66
KF_A	4.61	0.21	106.60	1.34	367.12	15.18

2.4. Composite Tooling and Composite Manufacturing

There are multiple methods for fabricating composite parts, each having their respective pros and cons. Traditionally in composite tooling, if a process is relatively expensive, time consuming, and utilizes expensive specialty materials then a high quality, a dimensionally accurate part is obtained. Conversely if a composite is manufactured rapidly at a low cost using a simpler method, large volumes of parts can be produced; however, these parts will have significantly less quality. The following section reviews the various methods for

producing composite tooling molds and the manufacturing processes used to fabricate composite parts using the tooling molds.

2.4.1. Composite Tooling

Composite tooling molds can be fabricated from virtually any material, provided the mold material is compatible with the composite part system and the mold is capable of withstanding the composite parts cure process. Traditionally, tooling molds were fabricated via casting or machining stock metals, pressing or forming for ceramics, or extruding and machining for plastics. The tooling mold material was chosen based on the CTE of the composites being formed, the number of parts to be formed, and the conditions required to cure the composite system. Ideally, Invar-36 is used for dimensionally critical parts due its low CTE (see section 2.1.2.1) however Invar-36 is expensive to machine and requires a long lead time. More often, tooling molds are manufactured out of stainless steel or various aluminum alloys (CTEs of ~18 μm/m°C and ~23 μm/m°C respectively) due to their availability and provided the dimensional requirements are not as critical as most aerospace applications [103]. Additionally, aluminum is relatively easy to machine compared to steel or Invar-36 [104]. Following the widespread adoption of AM, new opportunities for the fabrication of composite tooling molds were presented. Big area additive manufacturing (BAAM) techniques have made possible the production of full scale applicable parts from high temperature resistant thermoplastics such as acrylonitrile butadienestyrene (ABS), polyphenylene sulfide (PPS), polyetheretherketone (PEEK), and polyetherimide (PEI) resin to name a few [105]. Hassen et al) [106] demonstrated the use of FDM printing carbon

fiber reinforced PPS to manufacture large parts (>5.7 m^3) for composite tooling having good thermostability and sufficient mechanical strength (TS = 64.83MPa at 40% carbon fiber. However, these fabricated composite tooling molds required an additional surface finish prior to being subjected to an autoclave for forming an actual composite. The coupons formed on this tooling mold (post surface finish) after being subjected to the curing cycle within an autoclave process, displayed a maximum deformation of 0.381 mm, which is approaching the allowable tolerance of 0.25 mm for tier 1 aerospace composites [107].

In addition to using FDM for composite tooling, promising advances have been made toward metal AM techniques for the fabrication of composite tools. Indeed, metal tooling molds will have a significantly longer service life than their thermoplastic counterparts. Ding et al [108] demonstrated the practicality for producing a metal tooling mold via AM when they manufactured a Ti-6AL-4V tooling die via hybrid layer manufacturing (a form of DED). Other AM processes have machining capabilities already integrated into the system. These hybrid systems allow for the direct deposition of metal onto a compatible metal substrate to build the part while allowing the structure to be machined within the same system [109].

2.4.2. Composite Manufacturing

2.4.2.1. Hand Layup

Hand layup is the most common, least expensive method for fabricating composite parts. In hand layup, the fiber reinforcement is placed and resin is applied over the fiber matrix.

A commonly encountered industrial system is the carbon fiber/epoxy system [110]. Once the layer of fibers is saturated in resin, another layer of fibers is added, and the process is repeated until the desired number of layers have been applied. The molds used for hand layup are typically fiberglass composites due to their low cost. However, due to the inexpensive processing and lack of equipment involved in this process the quality of the resulting composites is far less than that of more expensive counterparts. The most notable differences in composite quality are observed in terms of the level of fiber saturation, density of microvoids present within the system, and the metrology of the surface [111].

2.4.2.2. Resin Infusion Processes

Resin infusion processes are similar to that of hand layup techniques except that a vacuum is pulled on the system to achieve a more efficient resin infiltration. Although this process is a cost effective system, it resin infusion processes typically has a low volume output [112]. There are many different variations of this vacuum infiltration system. The most popular infiltration systems are the Vacuum assisted Resin Transfer Molding (VARTM), the Seeman Composites Resin Infusion Molding Process (SCRIMP), and Autoclave techniques [113,114]. Generally, the mold along with the fiber reinforcement are placed inside a bag or sealed vessel. Then a vacuum is pulled on the system as the resin begins to saturate the fiber. Though these resin infusion processes are cumbersome and consist of multiple components, they are much more efficient in thoroughly infiltrating larger parts that are too large for hand layup methods. Figure 2.8 shows a diagram of a simple vacuum apparatus for a resin infusion process.

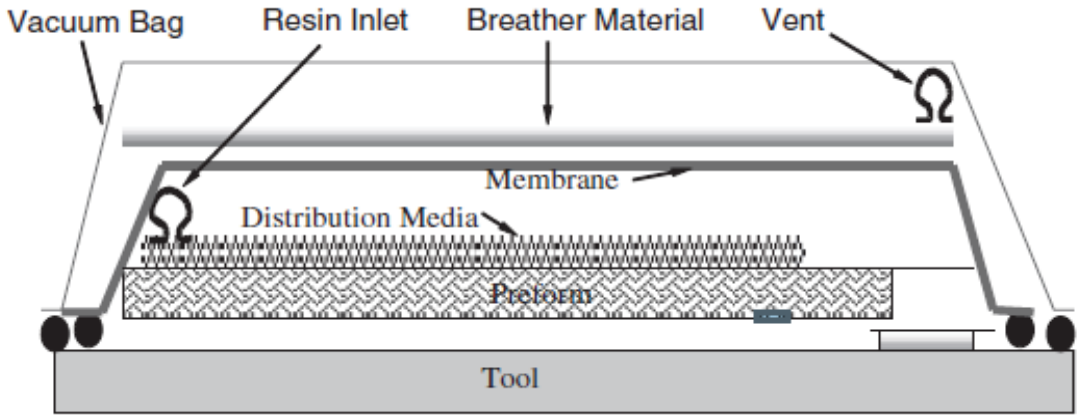

Figure 2.8: Vacuum bagging apparatus for resin infusion of composite parts

2.4.2.3. High Volume Molding

High volume molding of composites is similar to the injection and compression molding of metals and ceramics in that a compressive force pushes material through a tooling tie or into a mold chamber. Generally, in this process, a fiber reinforced resin is extruded through a heated tooling die or nozzle. The die is heated to allow the viscous resin to flow better.

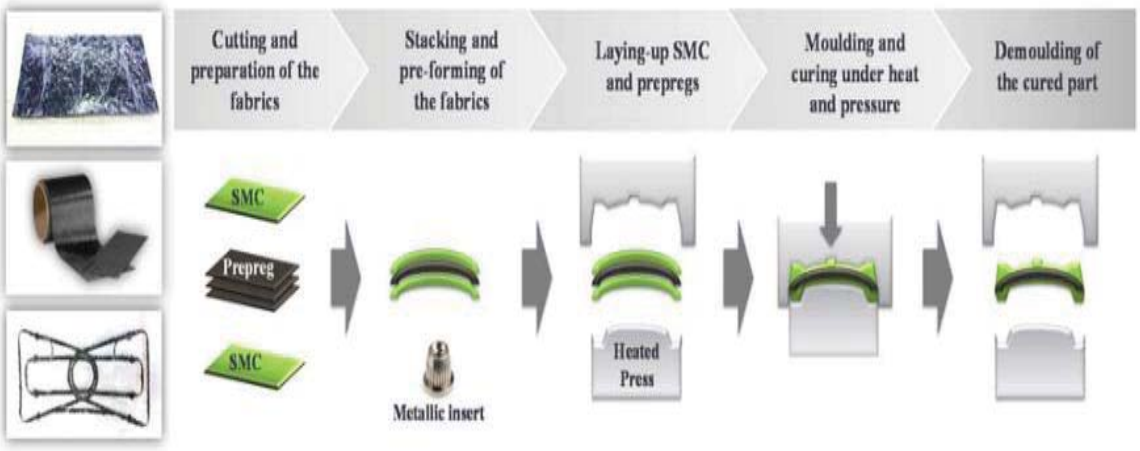

Figure 2.9: Flow diagram of the compression molding process for SMC composite materials [115].

Alternative large high volume molding is carried out through compression molding of sheet molding compounds (SMCs). SMCs are prepared by compressing a fiber reinforcement material between two sheets resinous paste. The Resulting SMC is then rolled to remove any entrained air and allowed to cure. Once cured, SMC sheets are cut down to fit the tooling mold, heated, and pressed until the part is molded. Figure 2.9 contains a schematic of the high volume compression molding machine.

SMC compression molding has cycle times of less than 1 minute per part. Tooling dies for these processes are very expensive so they are not recommended unless large volumes of parts (>10,000) are sought to be manufactured [115]. In addition to SMCs, bulk molding compounds (BMCs) are another commonly used material in the high volume molding processes. BMCs are fiber reinforced thermoset resins composites which do not fully cure until they are subjected to a certain temperature dependent on the specific thermos used. BMCs are manufactured by pre-impregnating (pre-preg) a fiber reinforcement material with a pre-catalyzed thermoset resin that is stable at room temperatures.

3. Experimental Methods

This chapter reviews the manufacturing and testing procedures conducted throughout this work. This research presents the different manufacturing processes investigated (direct casting, binder jetting and direct energy deposition) and the techniques and equipment used for the material analysis and characterization.

3.1. Manufacturing Process of Mold via Binder Jetting

3.1.1. Designing and Printing Process of the Mold, Core, and Gating System

The mold, core, gating and risers were designed on SolidWorks and flow simulations were performed in Magma. The system as a whole was designed as four separate parts: a bottom section, a middle section, a top section, and the core (Figure 3.1). The system was designed in a way that Invar would fill the mold from the bottom up until it was seen in the risers. This would suggest that Invar has filled the entirety of the mold.

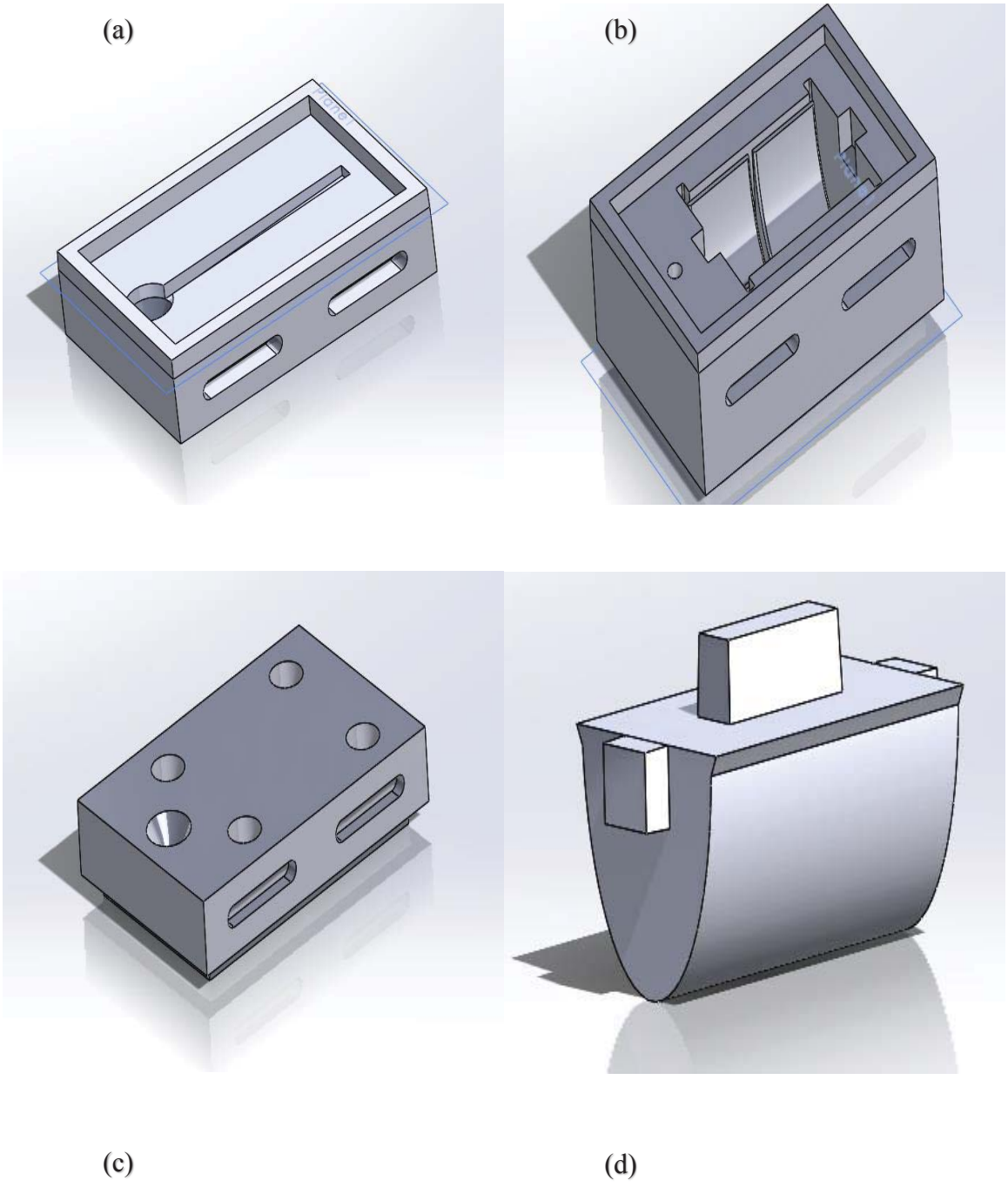

Figure 3.1: CAD drawings of the individual components for the total casting assembly: a) bottom drag section, b) middle cavity section, c) top section containing risers and sprue, and d) mold core.

All the mold parts were printed on an ExOne S-max binder jet printer (Humtown, Products) using silica sand a furan binder (see Figure 3.2). Once printed, the parts were depowdered and were ready to be assembled. This 3D printing process unlike other binder jetting methods does not require a post curing cycle to cure the material. Prior to assembly, silicone is deposited around the perimeter of each part where it shall be in contact with another part. The silicone acts as a sealant to ensure that parts are fitted together properly to prevent the Invar from leaking. Once assembled, the molds are ready for casting (see Figure 3.2).

Figure 3.2: ExOne S-max binder jetting printer (left) and the assembled printed mold (right).

3.1.2. Invar Casting

Invar-36 ingots were heated in an induction furnace to 1600°C. The furnace was mounted on a hydraulic tilt system, allowing the molten Invar to be poured directly into the sand mold once the pour temperature was reached. Figure 3.3 shows the casting apparatus prior to casting and the sand mold full of Invar after the cast.

Figure 3.3: Casting process: furnace used for melting the Invar-36 (left) and the mold after the cast of Invar-36.

The Invar was cast until it was observed overflowing in the risers as observed in Figure 3.3). Once cast, the part was allowed to ambiently cool overnight. Subsequently, the remainder of the sand mold was broken off and the cast Invar was obtained.

3.1.3. Post Processing

Post processing of the cast part involved the removal of the gating and risers and the polishing of the part. Figure 3.4 shows the cast Invar part after being removed from the sand mold with the gating and risers solidified and still attached.

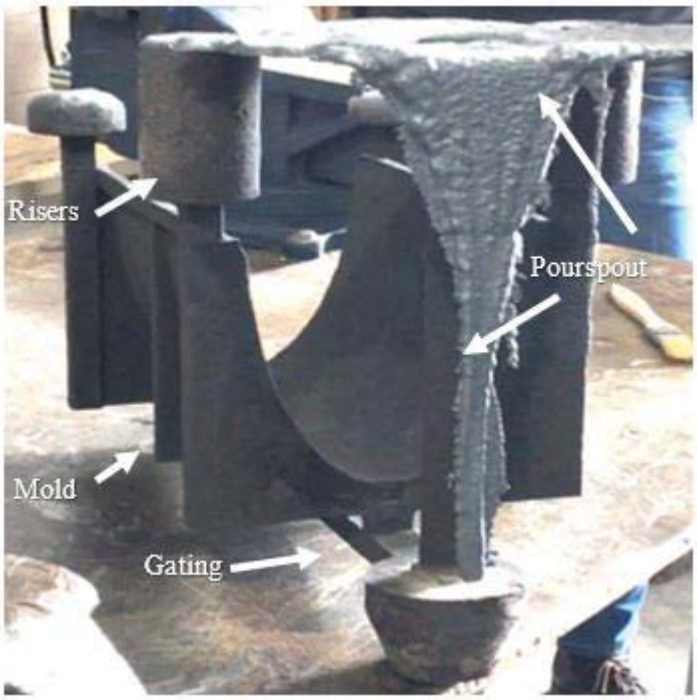

Figure 3.4: Cast Invar part after being removed from the sand mold with gating, risers and pour spout attached

3.2. Epoxy Infiltrated Ceramics

3.2.1. Materials and Binder Jetting

Silica (SiO_2) and zirconia (ZrO_2) sand were the two materials printed and studied in this process. The 3D printed silica had a porosity of 0.401 and a density of 1.34g/cm^3, while the 3D printed zirconia had a porosity of 0.372, and a density of 2.60g/cm^3. The porosity values were experimentally determined by contrasting images and measuring the ratio of solid material to voids within the sample (Figure 3.5).

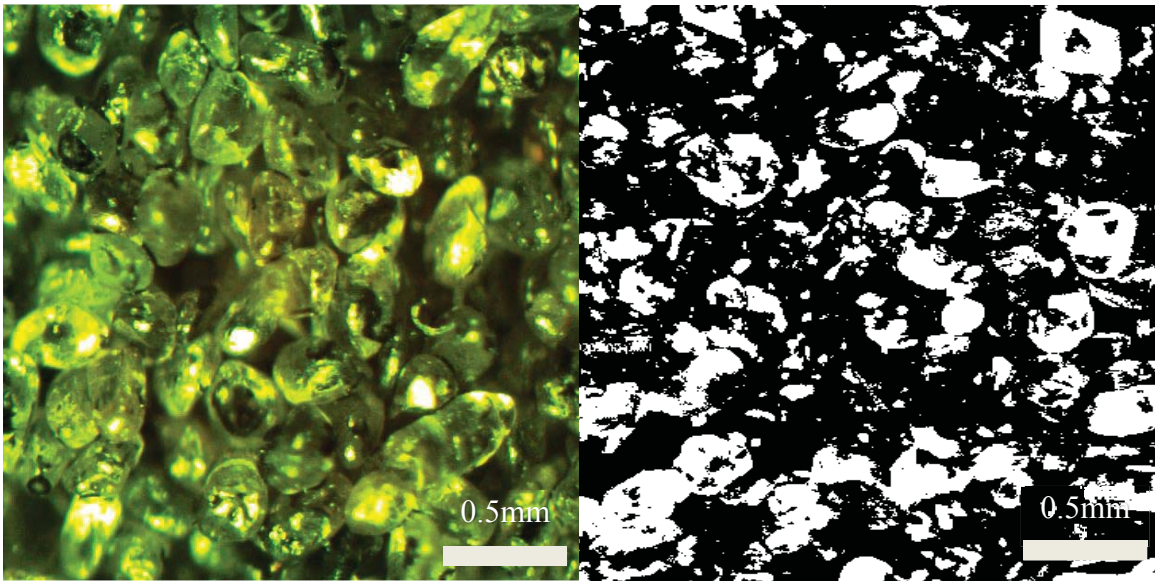

Figure 3.5: micrograph of as received zirconia from a light microscope (left) and greyscale version of the same image (right) used to determine porosity.

The epoxy used to infiltrate the porous ceramic parts was the TC-1614 A/B, a proprietary product purchased from BJB Enterprises. The TC-1614 A/B is a two-part low viscosity epoxy resin system designed to infiltrate and seal porous systems. The epoxy system was

prepared by mixing 5 parts of the resin (part A) with 1 part of the hardener (part B). Here, the materials were preheated separately prior to mixing then at 49°C for 15 minutes to reduce their viscosity. Once mixed, the work time was approximately 2 hours per 100g of material at 25°C.

The silica and zirconia were both printed on the aforementioned ExOne S-Max 3D sand. The S-Max printer has a maximum build volume of 1800mmx 1000mm x 700mm (L x W x H) and as previously mentioned, it uses an ExOne furan binder which does not require a post-curing step to obtain a rigid green state part [116]. Here, the silica had an average particle size of about 175 microns, while the zirconia had an average particle size of about 105 microns. Both materials were printed at a layer thickness of 280 microns. Once printed, the green state parts were depowdered and ready to be infiltrated. Figure 3.6 shows the CAD model as well as the printed tooling mold in its green state after being depowdered.

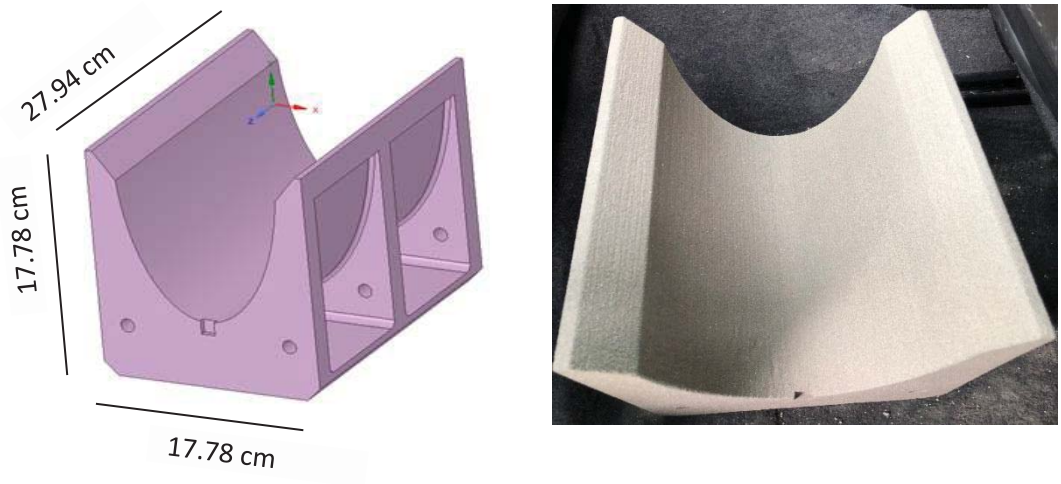

Figure 3.6: CAD model (left) and 3D printed zirconia sand part in its green body state (right).

3.2.2. Epoxy Infiltration and Cure Procedure

A vacuum infiltration system was used on the printed ceramic parts to achieve full infiltration. The vacuum infiltration setup consisted of a pump, pressure regulator, two valves, and a port to connect the pump to the bagging system (see Figure 3.7). The mold was placed inside of the vacuum bag, air was removed, and the epoxy was allowed to flow through it by using 20 in-Hg of vacuum. The vacuum was held for 15 minutes to achieve a complete infiltration. After the infiltration process, the system was allowed to cure following the supplier's recommendation curing protocol (see Table 3.1). Here, the tack free time for the infiltrated system was 5 hours at 49°C.

Figure 3.7: Vacuum infiltration set-up (left), and printed part during the infiltration process under vacuum (right).

Table 3.1: Curing cycle for the printed infiltrated samples. The total curing time was 6 hours.

Temperature	**Dwell (hr)**
66°C	2
121°C	2
149°C	1
177°C	1

In addition to the parts infiltrated with TC-1614 A/B, the silica and zirconia printed parts were infiltrated with four different resinous systems proprietary to Freshmade3D. These parts were infiltrated and cured per their optimized process.

3.3. Additive Manufacturing Methods

3.3.1. Direct Energy Deposition

Invar-36 powder and 316L stainless steel powder (both with a micron range between 10 and 45μm) were directly deposited onto a low carbon steel substrate. Both the Invar and 316L powders were purchased from LPW Technology Inc, (PA. US). Using a Hybrid Technologies direct energy deposition Ambit unit. The Ambit is essentially a CNC machine retrofitted with laser system allowing for direct deposition of powdered metals (see Figure 3.8)

Figure 3.8: Hybrid Technologies direct energy deposition Ambit system.

In this work, Invar was cladded to the 316L such that the Invar would serve as the work tooling edge and the 316L would make up the rest of the body (Figure 3.9).

Prior to printing the part, an initial investigation of the printing parameters for the Invar-36 and 316L stainless steel was performed in order to determine the best printing parameters for each material. After a series of tests, the following parameters (see Tables 3.2 and 3.3) were obtained.

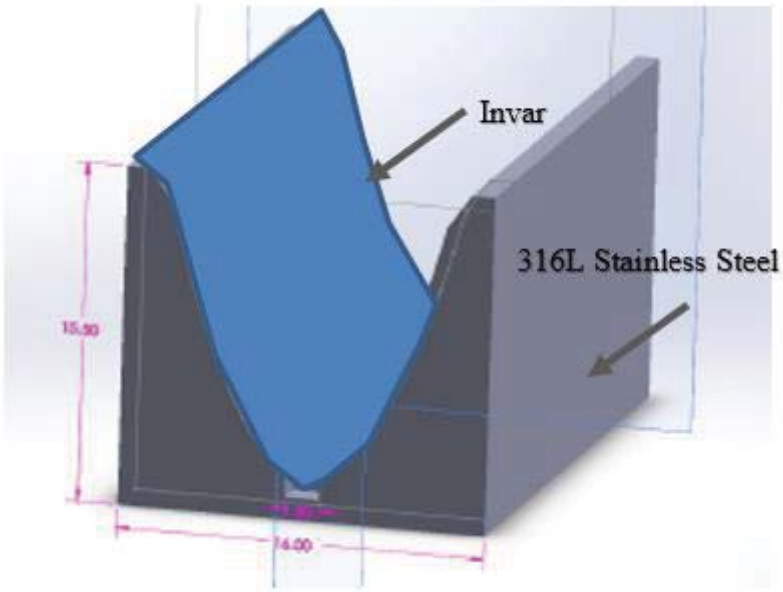

Figure 3.9: Cladding of Invar-36 to a stainless steel substrate.

Table 3.2: Printing parameter for the deposition of Invar-36on a Hybrid DED system.

Parameter	**Value**
Laser Power	395 W
Transverse Speed	350 (mm/min)
Deposition Offset (z-axis)	6 mm

Table 3.3: Printing parameter for the deposition of 316L on a Hybrid DED system

Parameter	Value
Laser Power	375W
Transverse Speed	205 (mm/min)
Deposition Offset (z-axis)	6 mm

3.4. Mechanical and Thermal Testing

3.4.1. Mechanical

Specimens were prepared for compression testing based on the ASTM C1358-13, while the flexural specimens in accordance to ASTM C1161-13. The tests were carried out in a 5500R series Instron system. Here, at least 5 samples of each specimen type were prepared for testing except for the specimens infiltrated with Freshmade3D resins. Here, only 3 specimens of each type of these were prepared. Figure 3.10 displays the dimensions of the specimens used for the mechanical testing.

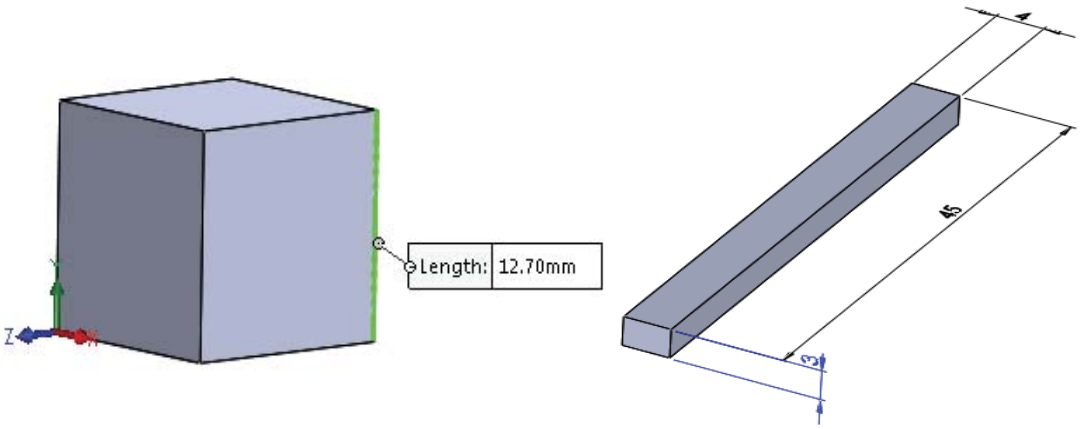

Figure 3.10: Schematics of the compression and flexural specimens used in this work.

A simple rule of mixtures (see equation 1) was applied to predict the resulting compression strength of the epoxy infiltrated system.

$$x_1\alpha_1 + x_2\alpha_2 = \alpha \quad (1)$$

Where x_i and α_i are the volume fraction and coefficient of compressive of each component respectively.

3.4.2. Thermal

A thermal mechanical analysis (TMA) was also carried out on the printed and infiltrated materials to determine their coefficient of thermal expansion (CTE). The testing was carried out on a TA Q400 system (courtesy of UDRI) using samples with dimensions of 20 x 5 x 5mm. The samples were ramped up to 185°C at a rate of 2°C per minute. The infiltrated composite tooling molds were also subjected to 10 heating cycles to investigate their dimensional stability. The thermal cycles consisted on heating the infiltrated tooling

to 177°C with a dwelling time of 20 min, and heating ramp of 5°C per min followed by a cooling stage where the infiltrated tooling was allowed to cool to ambient temperature. The dimensions of the parts were taken prior to the first heat cycle, as well as after each heating cycle. In addition, the CTE values of the epoxy-ceramic systems were predicted by applying a simple rule of mixtures (see equation 1). Where x_i and α_i are the volume fraction and coefficient of thermal expansion of each component respectively.

3.5. Material Analysis and Characterization

3.5.1. Optical and SEM Microscopy

Scanning electron microscopy (SEM) and optical microcopy was performed on all produced samples. The SEM was performed on a Jeol JIB-4500 Multi Beam SEM System with a LaB_6 electron source while the optical microscopy was carried out on a Nikon light microscope (Figure 3.11). In addition to SEM, energy dispersive spectroscopy (EDS) was performed on the aforementioned Jeol system, and on a Keysight 8500B FE-SEM unit (Figure 3.11).

Figure 3.11 : Jeol JIB-4500 Multi Beam SEM System (left) Keysight 8500B FE-SEM system (right).

3.5.2. X-Ray Analysis

X-ray diffraction (XRD) of the ceramic materials here investigated was performed on a Bruker AXS X8 Prospector. XRD is the scattering of X-rays by the regularly spaced atoms of a crystal lattice structure within a material system upon being energized with a high energy X-ray beam. With each material having a unique diffraction pattern, the X-rays are measured and the resultant diffraction is compared to a database of known diffractions to identify the crystal structure.

4. Results and Discussion

The following chapter presents and discusses the results obtained in this research work. The main objective of this study was to investigate different additive manufacturing technologies for producing a composite tooling mold. The first technology investigated was a ceramic binder jetting process, followed by a polymeric (epoxy) infiltration. The second approach was based on a casting process incorporating a 3D printed sand mold and the third approach used a Hybrid Technologies Direct Energy Deposition (DED) Ambit system for the cladding of Invar-36 across the working surface of a steel substrate.

4.1. Infiltrated Ceramic Tooling

4.1.1. Materials

Silica and zirconia ceramic systems were produced on an S-max 3D printer at Humtown Products (OH, US) (see sections 3.1.1-3.2.1 for printer specifications and printing process parameters). In this work, the silica had an average particle size of 175 microns (GFN ~83), while the zirconia had an average particle size of 105 microns (GFN 87-98). The porosity was found to be 0.401 and 0.372 for the silica and zirconia respectively. The density of the as received silica was 1.34 g/cm^3 while the density of the as-received zirconia was found

to be 2.60 g/cm^3. Figure 4.1 contains optical micrographs of the silica before and after the infiltration process.

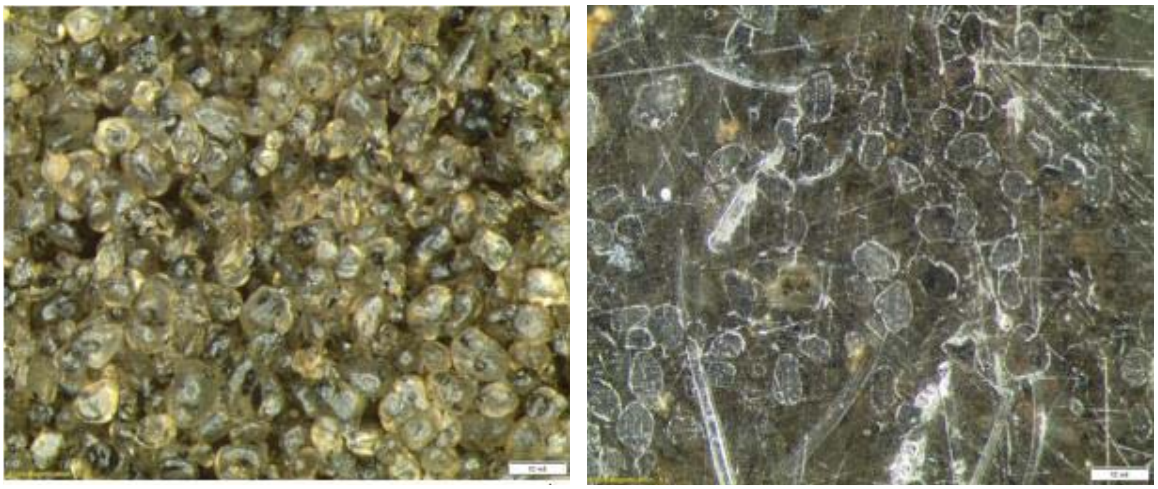

Figure 4.1: Optical micrograph of the as-received printed (non-infiltrated) silica sand (left) and the silica sand infiltrated with BJB (right).

The two ceramic materials were infiltrated with different epoxy resins. In total, there were ten epoxy infiltrated systems investigated in this work. Eight of which were infiltrated by Freshmade3D (4 silica and 4 zirconia) and two (one silica and one zirconia) infiltrated with a BJB Enterprises resin. Table 4.1 provides the ceramic systems investigated in the work. Included in the table are the silica and zirconia as-received (non-infiltrated) parts that were studied as controls.

Table 4.1: List of material investigated on the epoxy infiltrated ceramic tooling.

Material	Resin
Silica	none (control)
Zirconia	none (control)
Silica	BJB
Zirconia	BJB
Silica	#1
Silica	#2
Silica	#3
Silica	#4
Zirconia	#1
Zirconia	#2
Zirconia	#3
Zirconia	#4

4.1.2. Mechanical Testing

4.1.2.1. Compression Testing

The infiltrated and non-infiltrated (as-received) ceramic materials were tested under quasi-state compressive conditions. Figure 4.2 summarizes the compression data for each investigated system. From the figure, it is observed that the infiltrated system resulted in a superior compressive strength than that of the uninfiltrated ceramics. This suggests that the resin infiltration accounts for the increase in compressive strength of each system. From the figure, it is observed that the highest compressive stress was obtained from the silica sample infiltrated with resin #4 (150.1 MPa). This value is about 50 times higher than the non-infiltrated silica sample (2.9 MPa).

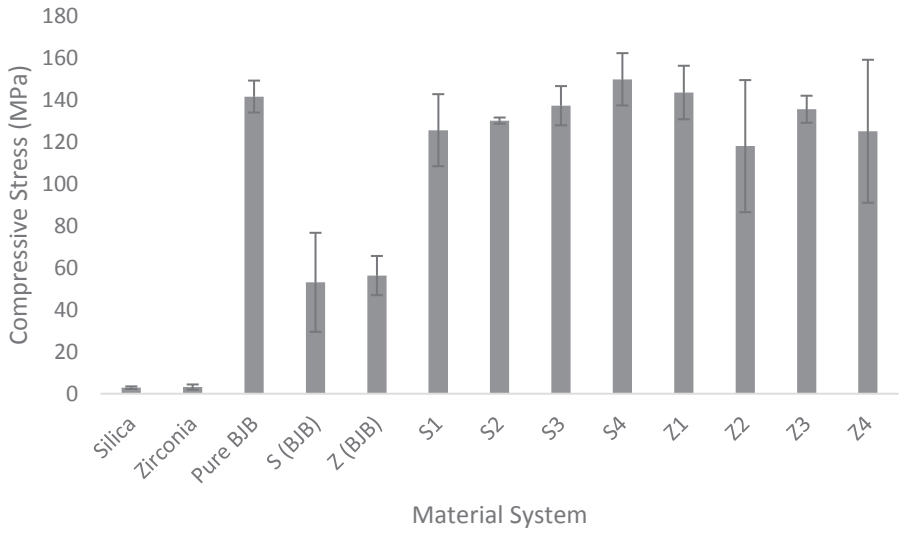

Figure 4.2: Summary of the compression results for the epoxy infiltrated ceramic systems and the as-received specimens. Here, "S" represents silica, and "Z" represents zirconia.

Included in the figure is the compressive strength of the pure BJB resin. The resin yielded a compressive strength of 141.8 MPa while the silica and zirconia infiltrated with BJB displayed compressive strengths of 53.2 MPa and 56.4 MPa, respectively. These results appear to follow a simple rule of mixtures (ROM). Thus, considering the porosities of the zirconia and silica (which was filled in by the epoxy resin) a ROM was applied to predict the compressive strength of the ceramics infiltrated with BJB. Table 4.2 presents the predicted ROM results for the compression testing

Table 4.2: Comparison of the measured compressive strength for silica and zirconia versus the theoretical compressive strengths determined from applying a simple rule of mixtures.

Material System	Compressive Strength Experimental	Compressive Strength Theoretical	Error
Zirconia as Received	3.2	-	
Zirconia BJB	56.4	54.7592	2.91%
Silica as Received	2.9	-	
Silica BJB	53.2	58.5989	10.15%
Pure BJB	141.8	-	

Table 4.2 shows that the predicted compressive strength of the silica and zirconia parts infiltrated with BJB resulted in 10.15% and 2.91% of error respectively. This suggests that a ROM can be used to predict the compressive strength of this type of infiltrated ceramic. The simple rule of mixtures was not applied to any of the Freshmade3D resins as the physical properties of the resin and the resin infiltration process are proprietary. It is interesting to note a large degree of standard deviation that was displayed in some of the infiltrated ceramic systems in Figure 4.2. This variability could be explained by the quality of infiltration process. Indeed, if any voids remain within the system following the epoxy infiltration, the probability of a premature failure increases, and consequently the actual strength of the system decreases. The compression profile of the as-received printed ceramics is shown in Figure 4.3. From the figure, it is observed that prior to infiltration, the as-received samples display a brittle failure mode once the material reaches their compressive strength.

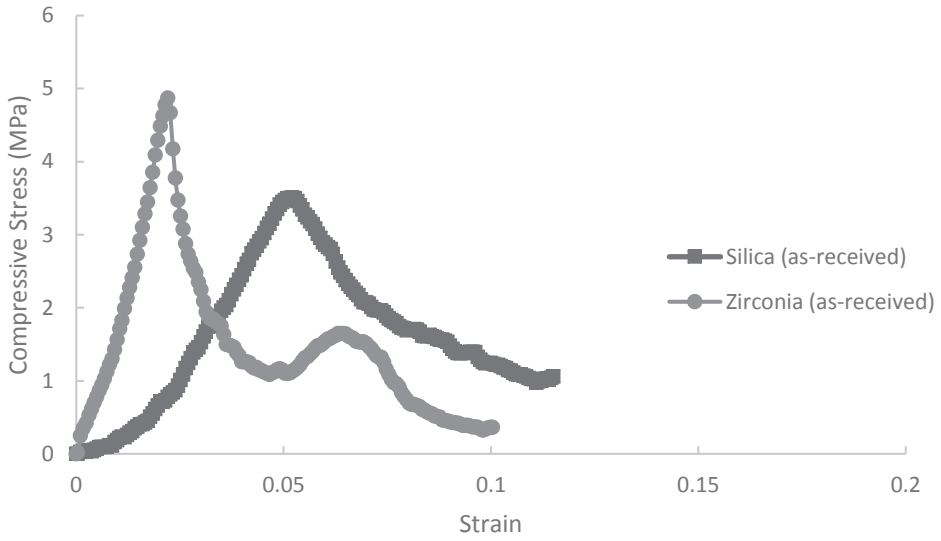

Figure 4.3: Stress-strain curves of the non-infiltrated (as-received) ceramic materials under compressive conditions

The brittle mechanism of the as-received samples was attributed to a crumbing effect of the samples after reaching their ultimate compressive strength. The stress-strain curves of the BJB infiltrated samples are shown in Figure 4.4. These infiltrated samples also appeared to display a brittle failure mechanism upon reaching their ultimate compressive strength. Here, no crumbling effect was observed, but rather a crack through the matrix was displayed. Similar behavior was observed on the ceramics infiltrated with the Freshmade3D resins.

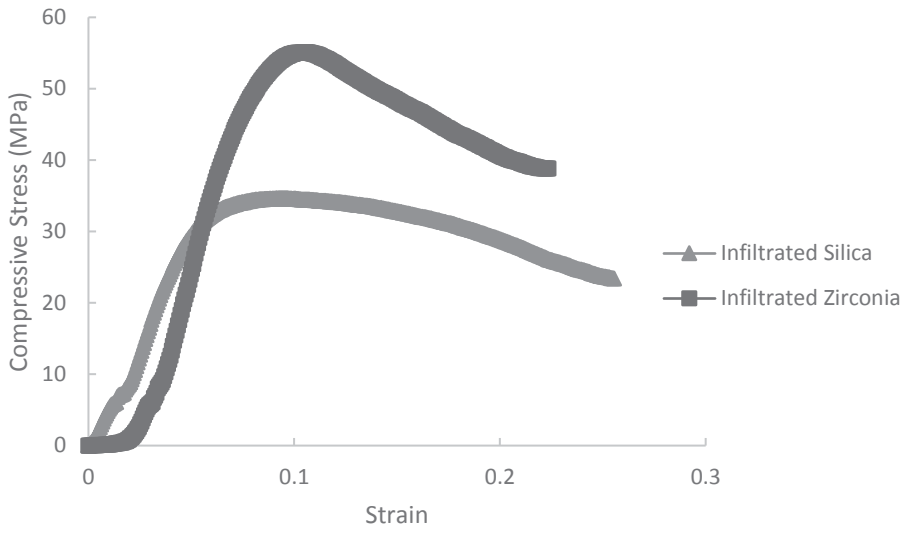

Figure 4.4: Stress-strain curves of the ceramic materials infiltrated with the BJB resin.

4.1.2.2. Flexural

In addition to the compression testing, flexural tests were also performed on the as-received and BJB infiltrated printed ceramics. Here, as on the compression testing, the as received ceramics essentially crumbled once the specimens reached their maximum flexural strength. Figure 4.5 shows the flexural strength for each of the investigated systems.

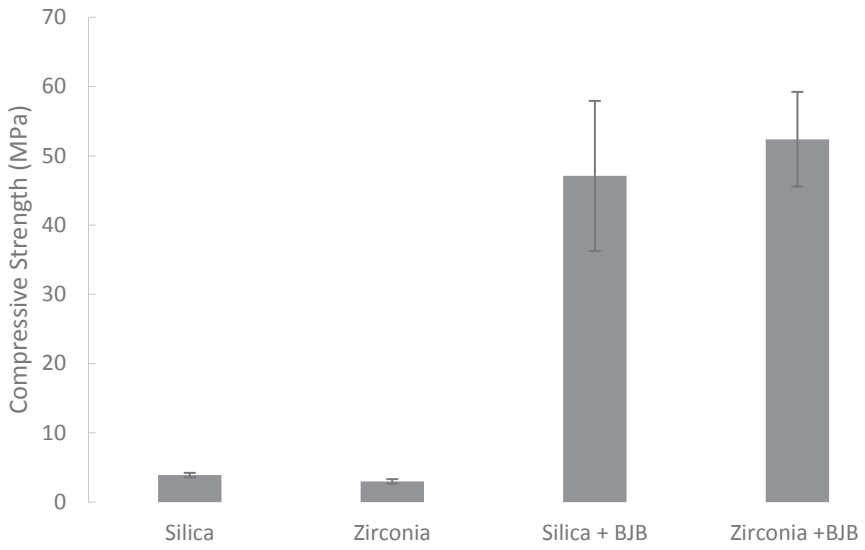

Figure 4.5: Flexural strength of the as-received and BJB infiltrated ceramics.

From the figure, it is clear that the increase in flexural strength is attributed to the epoxy infiltration. As in the case of the compression results, the epoxy infiltration seems to be the driving force behind the flexural strength of the tested samples. Here, the epoxy infiltration resulted in a flexural strength at least 12 times higher than the non-infiltrated systems. Also, as with the compression testing, the silica and zirconia systems displayed a brittle failure mode (see Figure 4.6).

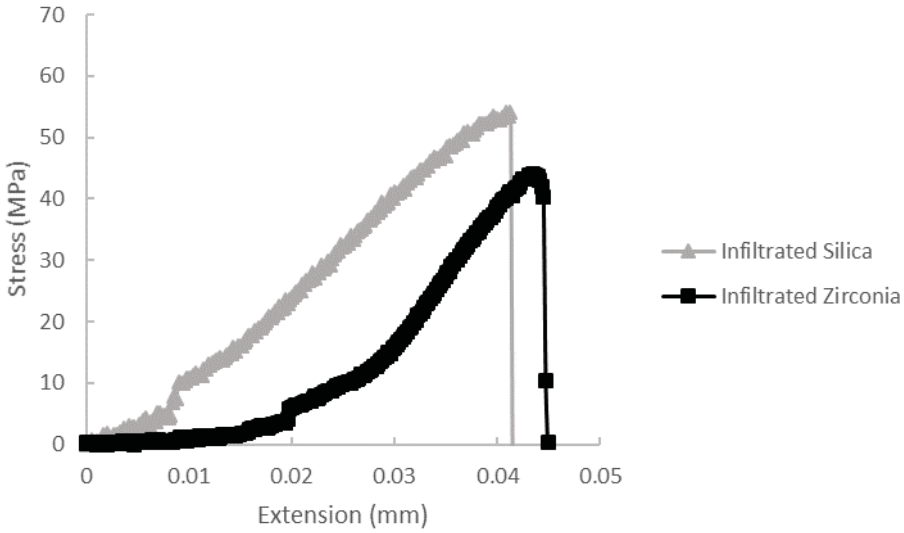

Figure 4.6: Stress-strain curves of the infiltrated samples under flexural testing conditions.

4.1.3. Microscopy and X-ray Characterization

4.1.3.1. As-received Samples

Optical microscopy and SEM characterization was performed on the as-received samples in addition to an EDS analysis. Figure 4.7 displays images of the as-received silica and zirconia materials.

Figure 4.7: Image of as-received silica (left) and zirconia (right) stock bars

Figure 4.8 shows an SEM micrograph and EDS analysis of the as-received silica system. From the figure, it is observed that the ceramic particles are covered in binder from the binder jetting process.

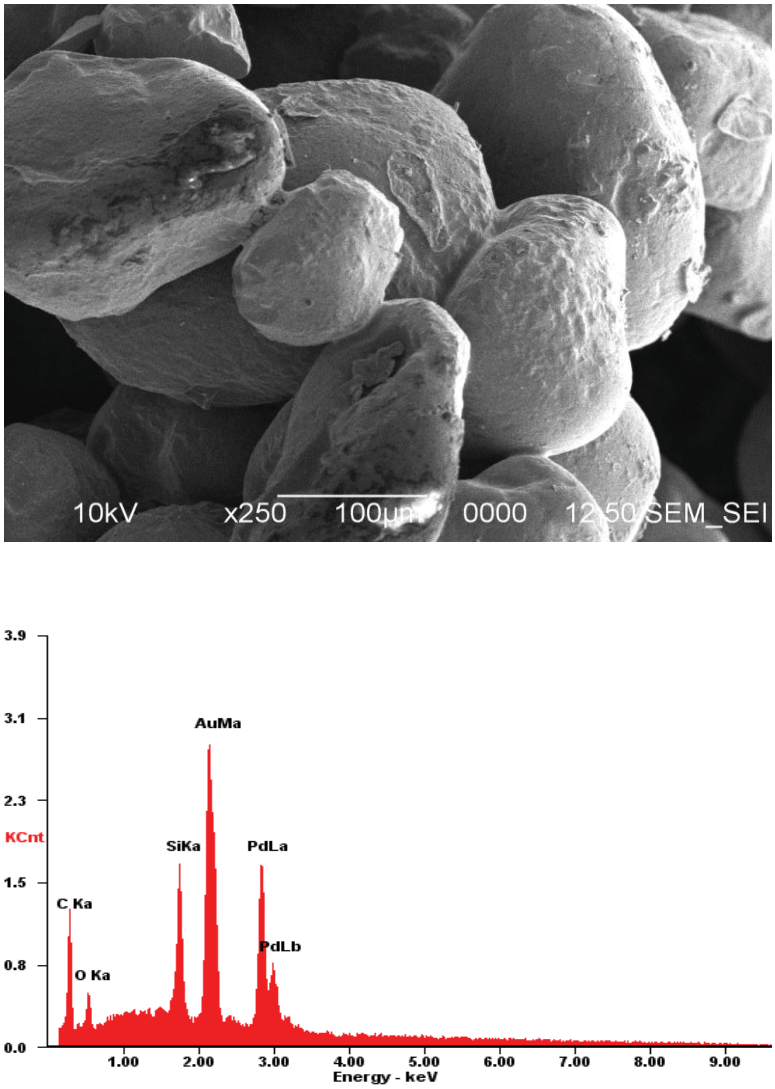

Figure 4.8Figure 4.8: SEM image of the as received silica particles covered with furan binder (top) and EDS results of the as received silica particles (bottom).

The presence of binder was confirmed through EDS analysis (see Figure 4.8). Here, the carbon peak at ~0.35keV is indicative of the binder since there were no other carbon containing substituents in the system other than the furan binder.

4.1.3.2. Infiltrated Samples

Optical microscopy and SEM was performed on the infiltrated samples. Figure 4.9 contains an image of the silica and zirconia compression samples infiltrated with the BJB resin.

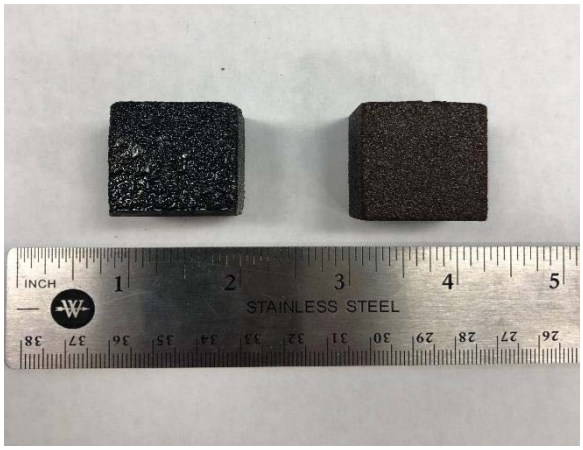

Figure 4.9: Optical micrograph of silica infiltrated with BJB resin (left), and zirconia infiltrated with BJB (right).

Further optical analysis, showed that the resin essentially serves as a "glue" as it infiltrates the pores within the ceramic samples. This is shown via an SEM micrograph of the as-received ceramic sample infiltrated with the BJB resin (see Figure 4.10). Similar observations were exhibited on all of the infiltrated systems investigated.

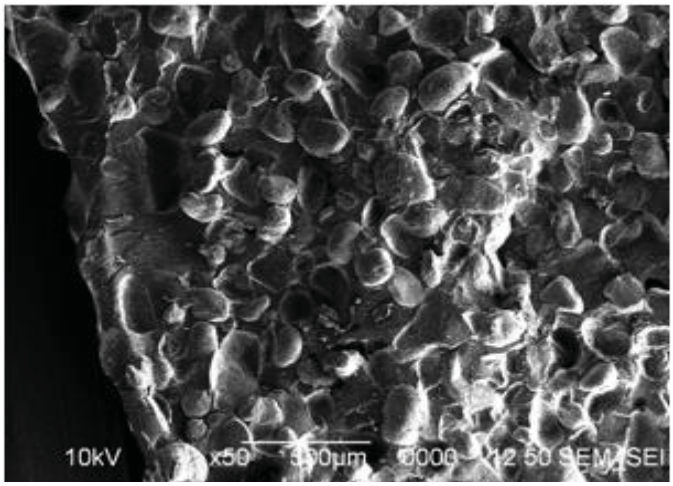

Figure 4.10: SEM micrograph of the silica infiltrated with BJB resin.

4.1.3.3. Fracture Analysis

SEM and optical microscopy was performed on the fractured as-received and infiltrated samples. Figure 4.11 shows an SEM micrograph of the fractured surface of an as-received silica flexural specimen.

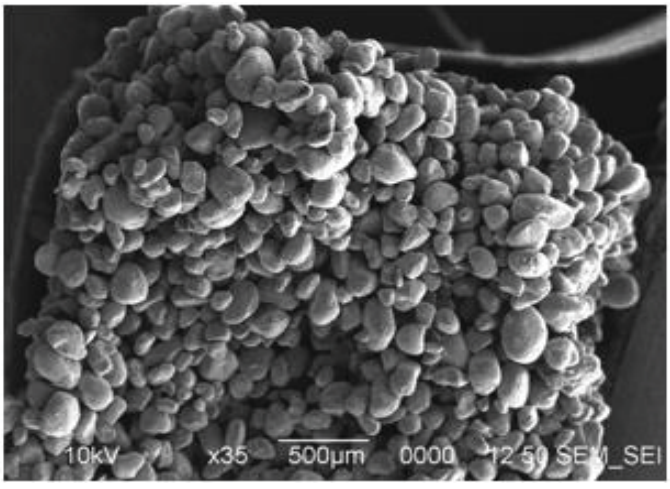

Figure 4.11: SEM micrograph of the fractured surface of the as-received silica sample following the flexural testing.

From the figure, it is observed that failure occurred between the adjacent particles by breaking the furan binder. Optical images of the fractured as-received samples under compression were omitted because upon reaching their compressive strength, they essentially crumble into a powder. In contrast, figure 4.12 provides a set of images of the infiltrated silica and zirconia samples infiltrated with Freshmade3D resins.

Figure 4.12: Images of infiltrated silica and zirconia. Silica #1 (a), silica #2 (b), silica #3 (c), silica #4 (d), zirconia #1 (e), zirconia #2 (f), zirconia #3 (g), and zirconia #4 (h).

From Figure 4.12 it is observed that all of fractured specimens have similar crack formations that propagate down into the center of the sample. This suggests that the epoxy infiltration may not have reached through the core of the sample. This phenomenon is particularly noticeable in Figure 4.12h, as a portion of the fracture surface has loose powder coming out of it. It should be noted that the fractured samples presented in this section are of 25.4 mm cubes and not the 12.7 mm cubes used for the actual compression testing.

Images of the fractured samples infiltrated with BJB resin are provided in Figure 4.13. From the figure, it is observed that the specimens have a fracture through the entire body in the direction that the load was applied rather than in a shear manner as observed on the samples infiltrated with Freshmade3D resins.

Figure 4.13: Fractured compression samples for silica infiltrated with BJB (left) and zirconia infiltrated with BJB (right).

It is interesting to note that although the fracture mechanism on the BJB infiltrated ceramics presented a columnar failure profile, which is expected to give a superior strength than the shear failure profile exhibited on the Freshmade3D infiltrated systems, it seems that the Freshmade3D resins had a superior mechanical performance compared to the BJB resin. An SEM analysis was also performed on the fractured surface of the flexural specimens. Figure 4.14 provides an SEM micrograph of a silica specimen infiltrated with BJB resin.

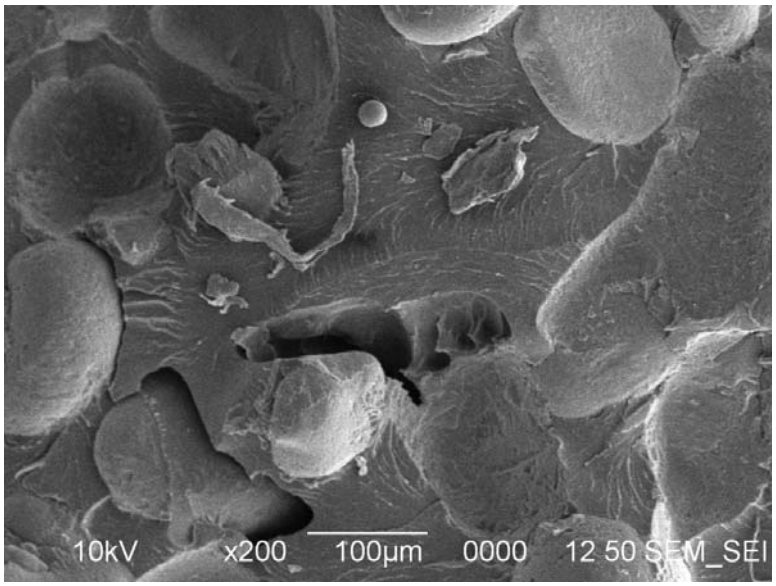

Figure 4.14: SEM micrograph of the fracture surface of a silica specimen infiltrated with the BJB resin.

This micrograph shows regions where the ceramic particles were dislodged, fissures formed, and residual particles cling to the surface. Additionally, contrary to the as-received material, the cured BJB resin is observed as the matrix with ridges and valleys resulting as a result of displacement during testing. The micrograph also confirms a brittle failure mode, since river patterns in the epoxy are observed [117]. In terms of crack propagation, the river patterns are pinched between cracks. The cracks are almost exclusively beside particles and particulate cavities. From the figure, it appears that the cracks are initiated at the epoxy particulate surface, followed by a brittle failure through the intermediate epoxy portions. Indeed, it seems that the cracks do propagate through the epoxy matrix, since the particles themselves are not fractured.

4.1.4. Thermal Testing

A thermal analysis was here performed in order to determine the coefficient of thermal expansion (CTE) for each ceramic system investigated. Table 4.4 contains the average CTE data of the epoxy infiltrated ceramic systems at a temperature range from room temperature (~22°C) to 185°C.

Table 4.3: Coefficient of thermal expansion results of the samples investigated.

Material	Sample Length (mm)	Average CTE (µm/m°C)
Z1	20.162	19.67
Z2	18.094	54.53
Z3	18.849	68.08
Z4	18.853	67.04
Zirconia as Received	19.166	2.9
Zircon + BJB	19.717	67.65
S1	19.955	28.11
S2	20.419	55.21
S3	20.739	76.93
S4	20.065	72.2
Silica as Received	19.992	13.26
Silica + BJB	19.992	72.2
Plain BJB	16.122	151.2

From Table 4.3, it was observed that the pure zirconia displayed the lowest average CTE (2.9 µm/m°C). The pure silica also displayed a low average CTE of 13.26 µm/m°C. However, neither of these as received ceramic systems in their green state can be directly used as composite tooling molds as they cannot withstand the curing pressures used on a typical autoclave process (~7 MPa) [118]. The epoxy resins, (though mechanically robust) had much higher CTE than the ceramic systems; therefore the ceramic/epoxy systems have a CTE between the pure ceramic and the pure epoxy material. Here it was recorded that the

BJB infiltrated systems have an average CTEs of 72.2 µm/m°C and 67.65 µm/m°C for the silica and zirconia, respectively. This is due to the high CTE of the BJB epoxy resin (160.5 µm/m°C). Here, a simple ROM was applied to predict the CTE of the infiltrated ceramics. The results are shown in Table 4.4. From the table, it is seen that the ROM predicts the CTE of the infiltrated system within a 10% of error.

Table 4.4: Comparison of experimentally determined CTE versus the theoretically

Material System	Average CTE (µm/m°C)	Average CTE (µm/m°C)	Error
	Experimental	Theoretical	
Zirconia as Received	2.9	-	
Zirconia BJB	67.65	60.94	9.92%
Silica as Received	14.28	-	
Silica BJB	72.2	72.91	0.98%
Pure BJB	160.5	-	

4.1.5. Composite Tooling

4.1.5.1. BJB Infiltrated Tooling

In this work, a composite tooling mold was fabricated based on both, the silica and zirconia infiltrated with the BJB resin. Images of these molds are provided in Figure 4.15.

Figure 4.15: Epoxy infiltrated 3D printed ceramic tooling molds. Zirconia infiltrated with BJB (left) and silica infiltrated with BJB (right).

Figure 4.15 shows that a relatively good infiltration was achieved on the fabricated tooling molds. These molds were subjected to 10 consecutive heating cycles up to 177°C in order to measure their dimensional stability. It was observed that after undergoing 10 heating cycles, the tooling molds remained without significant geometric deformation. In fact, it was observed that whereas the silica based tooling mold showed a 1.18% deformation in the inside diameter after 10 heat cycles, the zirconia tooling mold did not display any degree of deformation within a 0.1mm tolerance. This suggests a promising technology for producing composite parts, it should be noted that these tooling systems work up to ~180°C. Higher temperatures could degrade the epoxy resin and induce structural deformations in the composite. Tables 4.5 and 4.6 contains the measurements recorded throughout the thermostability study for each tool.

Table 4.5: Measurements from thermostability study for the silica lead edge tool.

	Silica					
Cycle #	Width (mm)	Height (mm)	Inside Diamter (mm)	% Change (W)	% Change (H)	% Change (ID)
0	177.8	177.8	152.5	-	-	-
1	177.8	177.8	152.5	0.00%	0.00%	0.00%
2	177.8	177.8	152.5	0.00%	0.00%	0.00%
3	177.8	177.8	153.5	0.00%	0.00%	0.66%
4	179.4	177.8	154.0	0.89%	0.00%	0.98%
5	179.4	177.8	154.0	0.89%	0.00%	0.98%
6	179.4	177.8	154.0	0.89%	0.00%	0.98%
7	179.4	177.8	154.0	0.89%	0.00%	0.98%
8	179.4	177.8	154.0	0.89%	0.00%	0.98%
9	180.2	177.8	154.0	1.34%	0.00%	0.98%
10	180.2	177.8	154.3	1.34%	0.00%	1.18%

Table 4.6: Measurements from thermostability study for the zirconia lead edge tool.

	Zirconia					
Cycle #	Width (mm)	Height (mm)	Inside Diamter (mm)	% Change (W)	% Change (H)	% Change (ID)
0	203.2	215.9	151.6	-	-	-
1	203.2	215.9	151.6	0.00%	0.00%	0.00%
2	203.2	215.9	151.6	0.00%	0.00%	0.00%
3	203.2	215.9	151.6	0.00%	0.00%	0.00%
4	203.2	215.9	151.6	0.00%	0.00%	0.00%
5	203.2	215.9	151.6	0.00%	0.00%	0.00%
6	203.2	215.9	151.6	0.00%	0.00%	0.00%
7	203.2	215.9	151.6	0.00%	0.00%	0.00%
8	203.2	215.9	151.6	0.00%	0.00%	0.00%
9	203.2	215.9	151.6	0.00%	0.00%	0.00%
10	203.2	215.9	151.6	0.00%	0.00%	0.00%

4.1.5.2. Freshmade3D Infiltrated Tooling

Based on the CTE recorded in this work (see Table 4.3), it was decided to produce a large composite tool using the zirconia material infiltrated with Freshmade3D resin #1. The CTE of the zirconia infiltrated with resin #1 was 19.67μm/m°C, a value significantly lower than the other ceramic/epoxy systems here investigated and even lower than that of aluminum (~23 μm/m°C), which is a material commonly used for composite tooling molds. The full scale zirconia tool infiltrated with the Freshmade3D resin #1 is shown in Figure 4.16. The tooling mold shows a good degree of infiltration as well as a smooth working surface.

Figure 4.16: Final zirconia tooling mold infiltrated with the Freshmade3D resin #1.

4.1.6. Fabricated Composites

A composite part was fabricated on the manufactured tooling molds infiltrated with BJB. Figure 4.17 shows the produced composites parts.

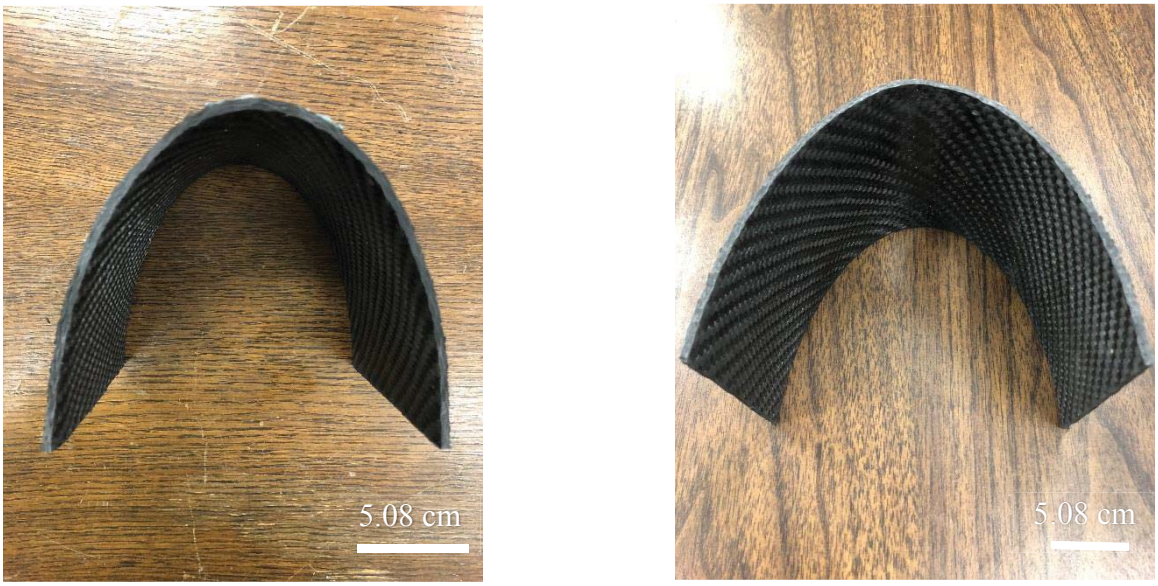

Figure 4.17: Lead edge composite parts formed on the BJB epoxy infiltrated 3D printed ceramic tooling molds.

Here, the composites were fabricated via common hand-layup process. An initial inspection of the fabricated composite seems to have resulted in a well consolidated structure. Optical microscopy was performed across the cross sectional area of the composite and it was observed that voids are present within the part (see Figure 4.18). However, these voids as well as any lack of quality observed in the fabricated composite parts are a result of the layup processed used and is unrelated to the quality of the tooling mold.

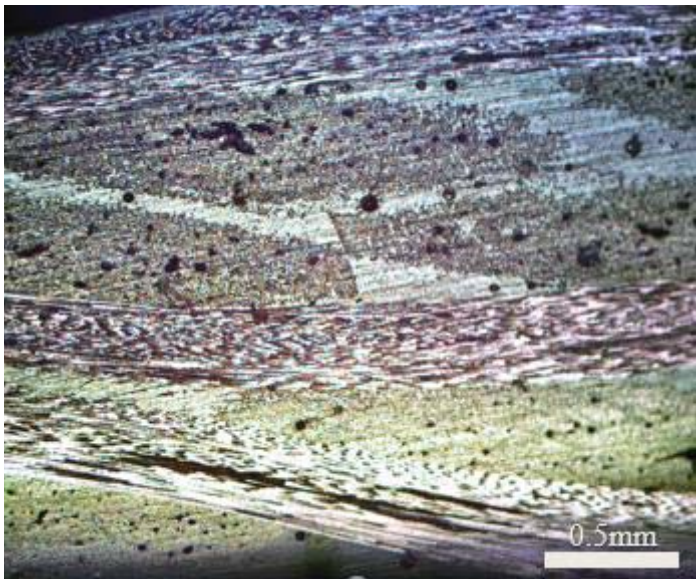

Figure 4.18: Micrograph of the cross section of the fabricated composite part.

4.2. Cast Invar Tooling

In this work, a composite tooling mold was printed from silica sand on the ExOne S-max system and subsequently cast into with Invar-36 alloy. After the casting, the mold was broken, the risers and gates were removed, and the final part was sand blasted to obtain a smooth surface finish. The cast part can be observed in Figure 4.19. Included in the figure is a SEM image of the cast Invar part; where it is observed that some voids are present. These voids seem to be associated with the gasification process that occurs during the metal casting. Snelling et al [119] observed similar results in their investigation of traditional no-bake sand molds versus 3D printed sand molds where they reported that the parts cast into the 3D printed sand molds had a higher porosity (1.59% porous compared to 0.65% porous, respectively) than the traditional sand mold materials due to the off-gassing of binder.

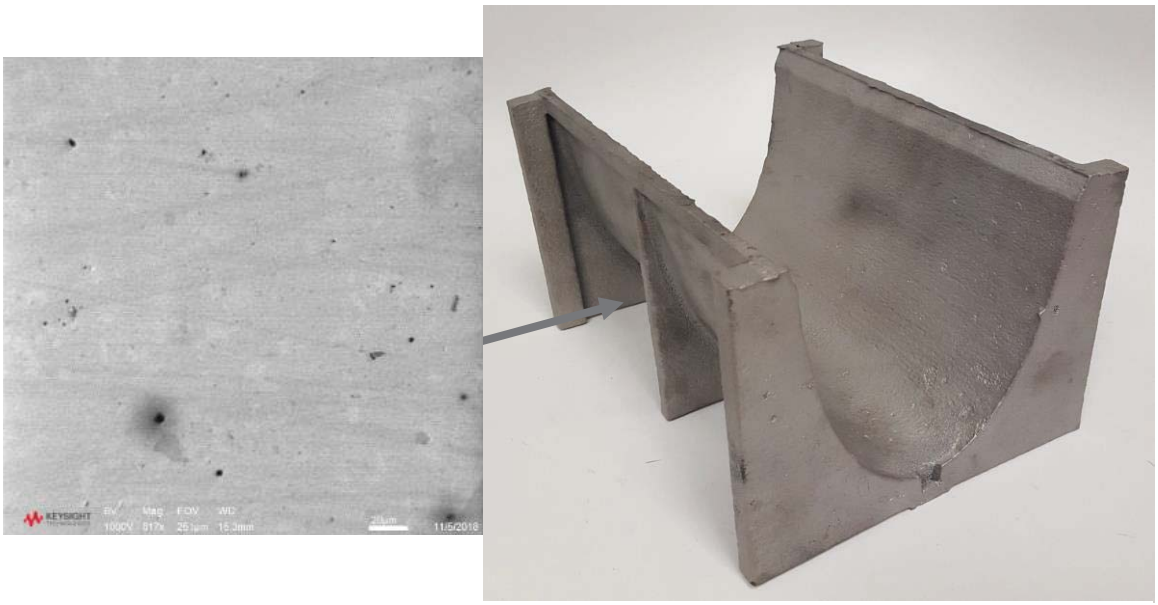

Figure 4.19: Final casted Invar-36 composite tooling mold. Included in the micrograph, is an SEM image of the casted Invar-36 material.

A metrology analysis was performed on the cast part (see Figure 4.20). It was found that the dimensional surface of the cast tool is 67.98% - 91.33% within a 0.015”- 0.030” tolerance, a range that satisfies the dimensional criteria required for the production CF/Epoxy systems for aerospace applications [120]. Further post-processing surface finish is required on the casted tool in order to comply with the manufacturing requirements [120].

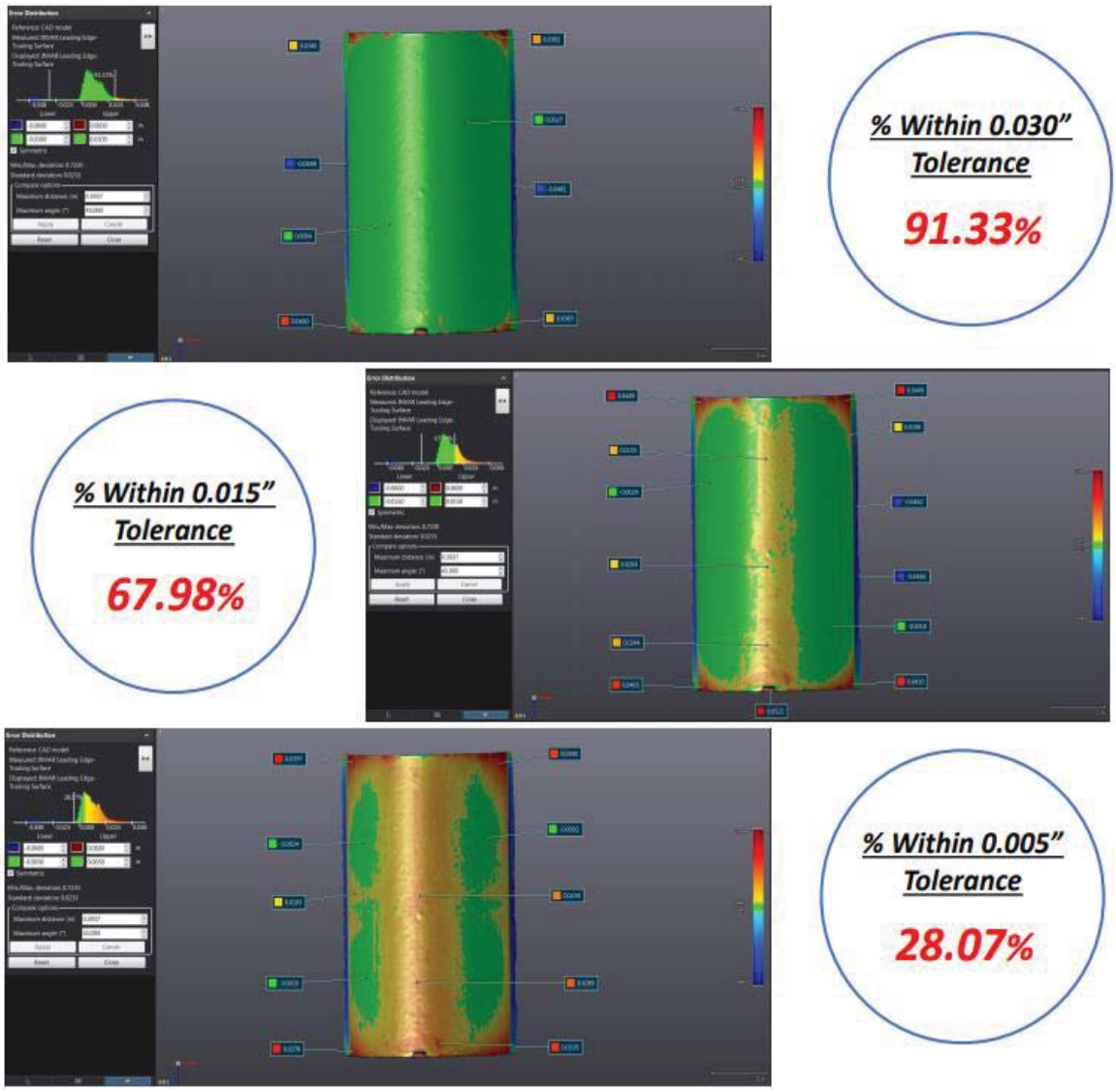

Figure 4.20: Results from the metrology analysis courtesy of the University of Dayton Research Institute (UDRI).

In addition to metrology, a CTE analysis was performed on the cast part (see Figure 4.21).

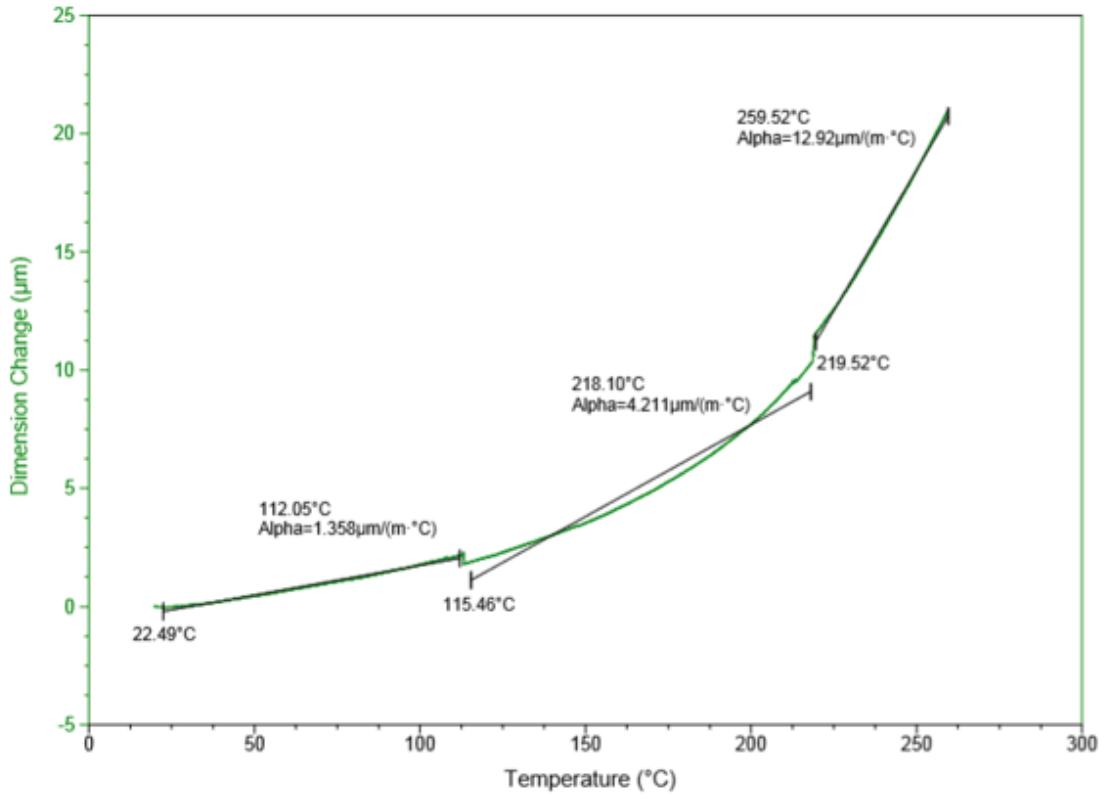

Figure 4.21: Recorded CTE data for the casted Invar system.

It was here observed that where the CTE of the cast Invar-36 was 4.21 µm/m°C up to a temperature of about 220°C. A CTE three times lower was recorded within a temperature range of 22.5°C and 115°C. This clearly shows the unique thermal features of Invar-36 being used for composite tooling applications. In contrast, the CTE of the Invar at 260°C was nearly three times greater than at 220°C. This result is due to the exposure of Invar-36 to a temperature above its curie point (230°C). The curie point of material is the temperature at which the material loses its permanent magnetic properties. As discussed in section 2.1.2.1, Invar-36 displays a low CTE of about 3.6 µm/m°C, due to a phenomenon known as the "Invar Effect". The "Invar

Effect" is essentially two physical mechanisms of invar; the normal lattice expansion and the anomalous contraction due to the spins of the excited Fe atoms. However, once Invar is subjected to temperatures greater than that of its curie point, the anomalous contraction ceases and the material expands at a rate more typical for that of a steel (~12 μm/m°C). In this work, the average CTE of the Invar-36 was 3.93 μm/m°C which is similar to the values found in literature for an Invar-36 (CTE of 3.6 μm/m°C up to around 200°C) [57]. Here, the CTE of the cast Invar-36 was averaged up to 220°C since CF/Epoxy composites are typically cured around 175°C [12]. An x-ray analysis was also carried out on the cast Invar-36 part. Figure 4.22 shows the XRF and XRD results for the cast Invar system.

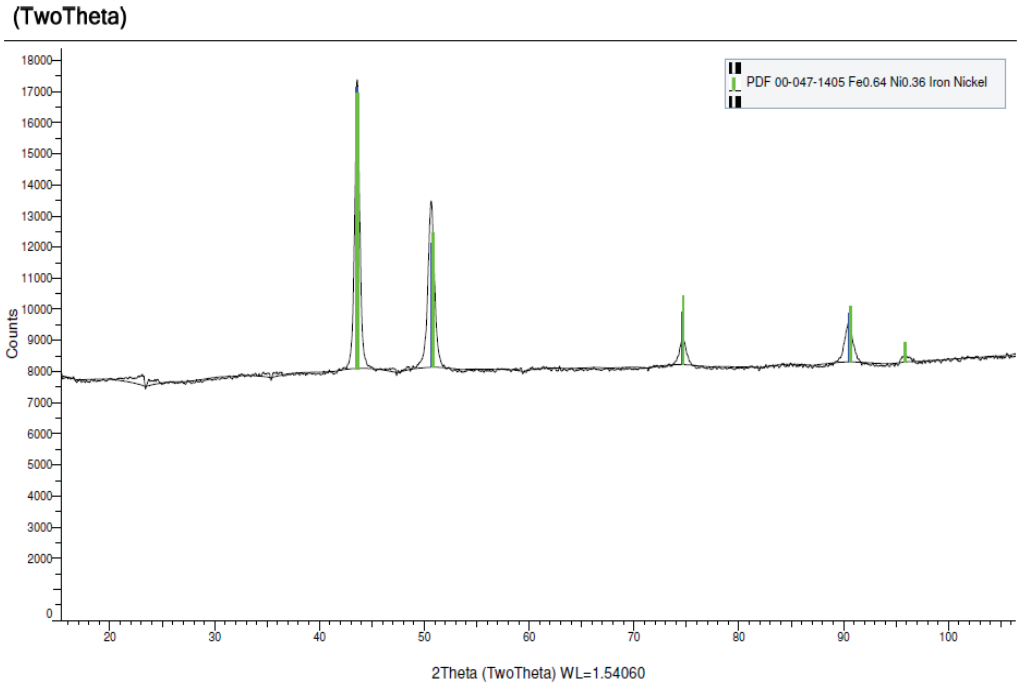

Element	Fe	Ni	Other
Composition	63.427	32.651	3.921

Figure 4.22: X-ray diffraction (XRD) analysis results (top) and X-ray fluorescence (XRF) results (bottom).

From the figure, it was determined that the system is composed of the Ni-Fe alloy with a composition of 64% Fe and 36% Ni. The XRF analysis shows the elemental composition of the cast Invar where it is observed that the Fe is 63.4% and the Ni is 32.6%. These results seem to concur with the CTE results measured on the cast Invar sample where a CTE of 3.93 µm/m°C was reached. This results suggests that a successful low CTE cast Invar-36 part can be obtained using a 3D printed sand mold.

4.3. Hybrid Manufactured Tooling

This portion of the research work investigated the cladding of Invar-36 to the surface of a 316L stainless steel mold. This allows for the remainder of the body to be printed out of a less expensive material such as commercial steel. This process was performed on a Hybrid Technologies Ambit system using a DED technology. This process could result in a potential cost savings approach due to the reduced amount of Invar required as compared to a casting of pure Invar alloy. An SEM image of the Invar-36 as a powder is shown in Figure 4.23 where it is observed that the average particle diameter is about 12 μm.

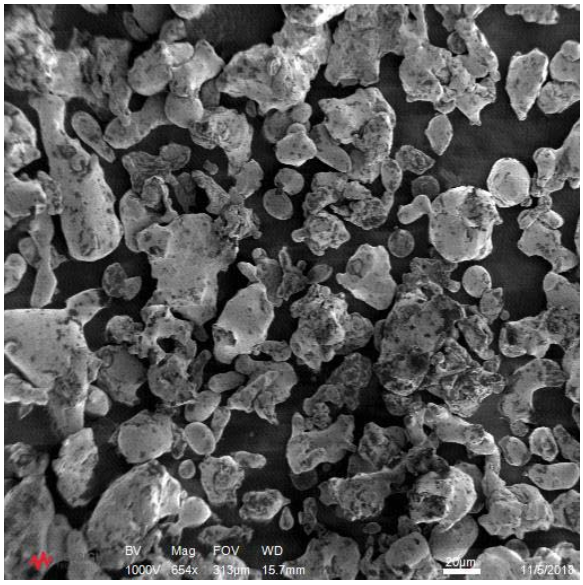

Figure 4.23: SEM micrographs o Invar-36 powder in its as-received form.

The Invar-36 powder as well as 316L powder were deposited onto a steel plate to evaluate their 3D printing process parameters. Figure 4.24 shows the layered part of the 3D printed hybrid structure.

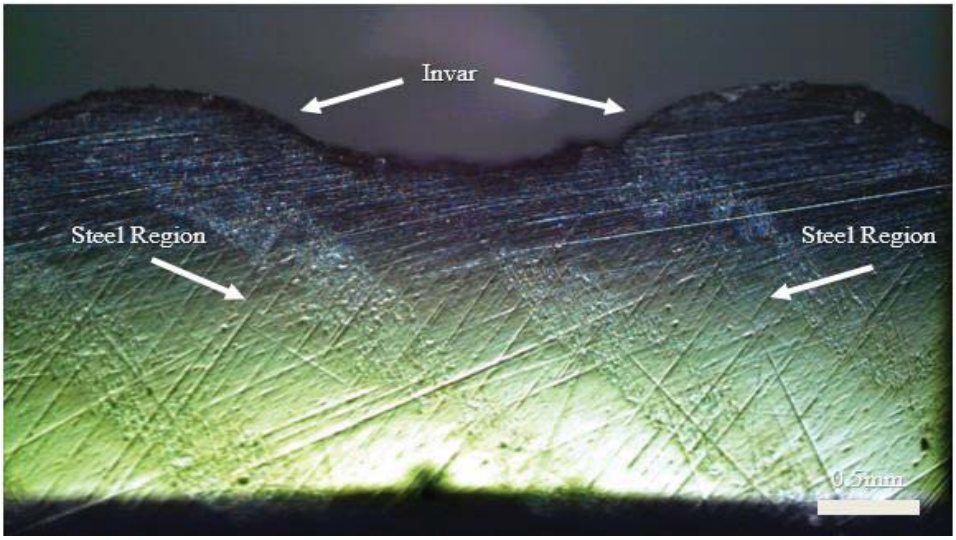

Figure 4.24: Cladding of Invar-36 to a stainless steel substrate.

As it can be seen in Figure 4.24, a relatively good layer process was here achieved. The printed Invar-36 was further analyzed a SEM (see Figure 4.25) where it was observed that the Invar-36 was clearly sintered however it was relatively porous compared to the cast Invar-36 (see Figure 4.19). This porosity can be attributed to the direct energy deposition process itself as similar results were had in Angelastro et al's [121] work where they observed Colmonoy-227F parts manufactured via direct metal laser deposition had measured density range of 96.6% - 97.7% relative to the bulk material.

A XRD analysis was performed on the printed sample (see Figure 4.25). Here it was observed that the resultant deposited Invar was in fact Invar-36 as a 36 wt% Ni content was recorded.

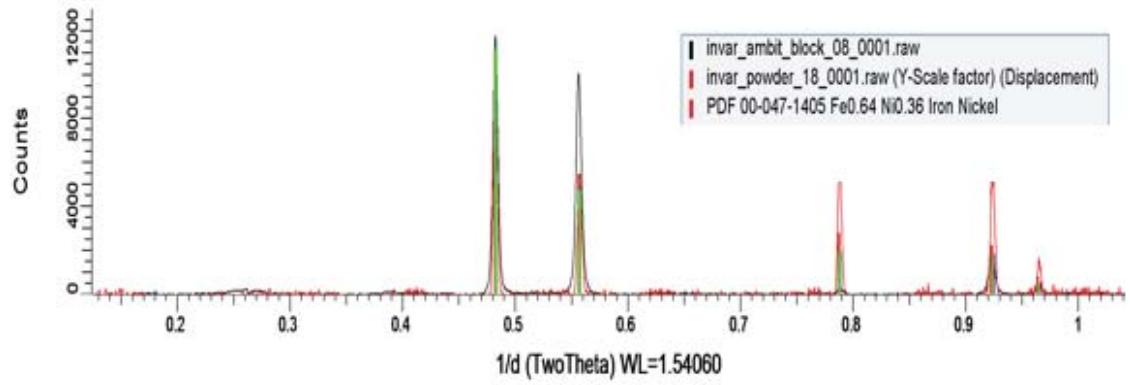

Figure 4.25: XRD results of the Invar-36 printed via DED

Based on the preliminary data of the scaled cladding samples, a larger composite tooling structure (40.64 cm x 40.64 cm) was investigated in the Ambit system. Figure 4.26 shows the STL file of the proposed tooling mold design.

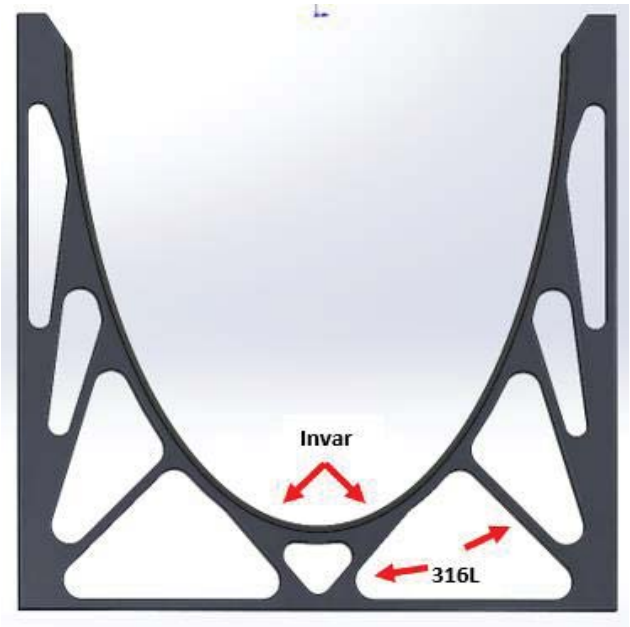

Figure 4.26: CAD drawing of the proposed Invar-36 cladded over 316L stainless steel tooling.

An initial thermo-mechanical simulation based on the CTE of each material was performed to predict the deflection of this hybrid system. Here, three different systems were modeled: a pure steel system, a pure Invar system, and the steel system cladded with 4 mm of Invar. Figure 4.27 and Table 4.8 display the FEA deflection profile and dimensions from the predicted deflections for each system.

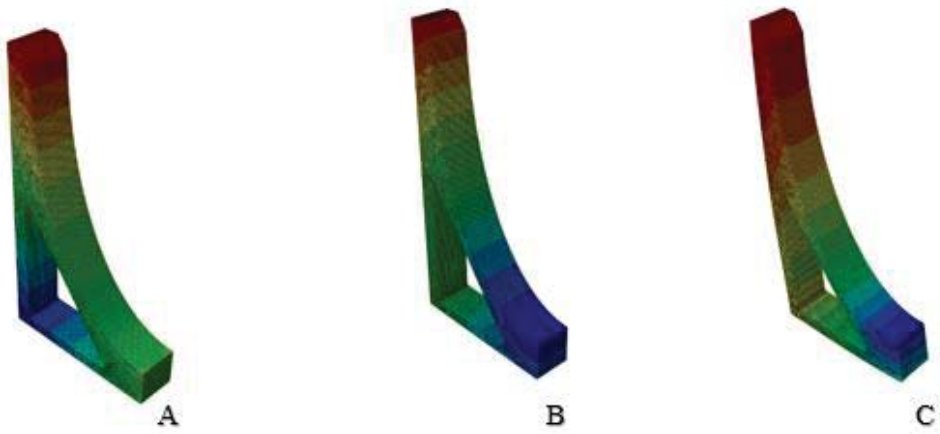

Figure 4.27: Predicted deflections for the composite tool manufactured via DED. The systems were steel-steel (a), invar-invar (b), and steel-invar (c).

Table 4.7: Maximum predicted deflections for the tool measured across the upper section.

System	Maximum Observed Deflection (mm)
Steel-Steel	4.19
Invar-Invar	1.01
Steel-Invar	1.32

The maximum deflection was measured at the tips of the lead edge tooling mold which is observed as the dark red regions in the FEA images. The Steel-Steel system displayed the largest overall deflection (4.19 mm). It was expected that this system would have the largest deflection considering 316L stainless steel has a CTE of ~18.2 μm/m°C up to 500°C. Invar is particularly known for it's near zero CTE (2.9 and 3.66 μm/m°C) and as expected, the Invar-Invar system displayed the least deflection (1.01 mm). Upon cladding the leading edge (working surface) of the 316L SS tooling mold with 4 mm of Invar, the

overall surface deflection resulted in a maximum of 1.32 mm, 68.4% less than the Steel-Steel system. The predicted date from the thermo-mechanical simulation suggests that this cladding process via DED could be a promising manufacturing process for composite tooling molds.

5. Conclusion

These additive manufacturing processes were investigated in this research program in order to produce a low coefficient of thermal expansion lead edge composite tooling mold to be used in to 180°C temperature range. Three different composite tooling molds were successfully manufactured in this work. One of the processes consisted of infiltrating a 3D printed ceramic mold manufactured via binder jetting with an epoxy resin (A). The second method consisted of casting Invar-36 into a 3D printed silica sand mold (B). Lastly, the third process investigated was the based on the cladding of Invar-36 to a 316L stainless steel substrate through a direct energy deposition process (C).

A) Here, multiple ceramic epoxy systems were investigated with the most promising system was zirconia sand infiltrated with Freshmade3D resin #1 (CTE 19.67 μm/m°C). Although this CTE is greater than that shown by carbon fiber epoxy systems and Invar-36 tools (2.9-3.66 μm/m°C and 3.6 μm/m°C, respectively) it is comparable to that exhibited by aluminum tooling (~23 μm/m°C) which is a material commonly used to fabricate composite tooling. A successful carbon fiber /epoxy composite part was produced using the manufactured tooling mold. This manufacturing method appeared to yield a tooling mold with a CTE higher than required for carbon fiber epoxy composites. However, this technology can have a lead time of less than a week compared to a lead time of 2-3 months for aluminum.

B) This process resulted in an Invar-36 mold with a CTE of 3.93 μm/m°C which is comparable to that exhibited by carbon fiber epoxy composites. This tooling mold

displayed a surface stability of 67.98% - 91.33% within a 0.015” – 0.030” tolerance and has a much shorter lead time than a traditionally machined Invar-36 or aluminum tooling mold.

C) This process seems to represent a promising approach for producing an inexpensive composite tooling mold with a low CTE where only the specialty Invar-36 alloy is cladded on the work surface area of the tool. Current work is being performed to further investigate this technology.

The present work has shown that additive manufacturing can be used to successfully fabricate composite tooling with low CTE’s in the range of 180°C capable of producing dimensionally accurate carbon fiber/epoxy composite parts. Future works would further investigate the hybrid additive manufacturing technology in order to deliver a usable composite tooling mold. Additional future works would look to replace traditional aluminum tooling with the epoxy infiltrated ceramic method discusses here within and analyze the quality of the resulting composite. Lastly, other future works may investigate the binder jetting post processing of low CTE materials such as fused silica and other ceramic based, powdered materials for use as composite tooling.

One such future work that seems promising is an SLA process for printing fused silica. These silica specimens are further post processed, sintered, and then transformed via a metal infiltration technique to form a ceramic-metal composite tooling having impressive mechanical and thermal properties that could satisfy aerospace tooling requirements.

References

1. "Composite Tooling Market to Reach More than US$550 Million." *Reinforced Plastics*, vol. 61, no. 3, May 2017, p. 131. *Crossref*, doi:10.1016/j.repl.2017.04.052.
2. "Composites Industry Market Overview." *American Composites Manufacturers Association*, https://acmanet.org/composites-industry-overview/. Accessed 18 Oct. 2018.
3. Zweben, Carl. "Advances in Composite Materials for Thermal Management in Electronic Packaging." *JOM*, vol. 50, no. 6, June 1998, pp. 47–51. *Crossref*, doi:10.1007/s11837-998-0128-6.
4. Salonitis, Konstantinos, et al. "Multifunctional Materials: Engineering Applications and Processing Challenges." *The International Journal of Advanced Manufacturing Technology*, vol. 49, no. 5–8, July 2010, pp. 803–26. *Crossref*, doi:10.1007/s00170-009-2428-6.
5. Bowles, David E., et al. "Prediction of Coefficients of Thermal Expansion for Unidirectional Composites." *Journal of Composite Materials*, 1989.
6. Das, S. The Cost of Automotive Polymer Composites: A Review and Assessment of DOE's Lightweight Materials Composites Research. ORNL/TM-2000/283, 777656, 26 Jan. 2001. Crossref, doi:10.2172/777656.
7. Giolli, C., et al. "Wear Resistance Improvement of Small Dimension Invar Massive Molds for CFRP Components." Journal of Thermal Spray Technology, vol. 18, no. 4, Dec. 2009, pp. 652–64. Crossref, doi:10.1007/s11666-009-9397-z.

8. *Capabilities - Rotating Composite Technologies*. http://rotatingcomposites.com/capabilities.html. Accessed 25 Aug. 2018.
9. Wang, Wanlong, et al. "Rapid Tooling for Sand Casting Using Laminated Object Manufacturing Process." *Rapid Prototyping Journal*, vol. 5, no. 3, Sept. 1999, pp. 134–41. *Crossref*, doi:10.1108/13552549910278964.
10. Jr, Flake C. Campbell. *Manufacturing Technology for Aerospace Structural Materials*. Elsevier, 2011.
11. Potter, K. D., et al. "The Generation of Geometrical Deformations Due to Tool/Part Interaction in the Manufacture of Composite Components." Composites Part A: Applied Science and Manufacturing, vol. 36, no. 2, Feb. 2005, pp. 301–08. ScienceDirect, doi:10.1016/j.compositesa.2004.06.002.
12. Davies, L. W., et al. "Effect of Cure Cycle Heat Transfer Rates on the Physical and Mechanical Properties of an Epoxy Matrix Composite." Composites Science and Technology, vol. 67, no. 9, July 2007, pp. 1892–99. ScienceDirect, doi:10.1016/j.compscitech.2006.10.014.
13. Huang, C. K., and S. Y. Yang. "Warping in Advanced Composite Tools with Varying Angles and Radii." Composites Part A: Applied Science and Manufacturing, vol. 28, no. 9–10, Jan. 1997, pp. 891–93. Crossref, doi:10.1016/S1359-835X(97)00045-6.
14. Conner, Brett P., et al. "Making Sense of 3-D Printing: Creating a Map of Additive Manufacturing Products and Services." *Additive Manufacturing*, vol. 1–4, Oct. 2014, pp. 64–76. *Crossref*, doi:10.1016/j.addma.2014.08.005.

15. Rayna, Thierry, and Ludmila Striukova. “From Rapid Prototyping to Home Fabrication: How 3D Printing Is Changing Business Model Innovation.” *Technological Forecasting and Social Change*, vol. 102, Jan. 2016, pp. 214–24. *Crossref*, doi:10.1016/j.techfore.2015.07.023.

16. Bourell, David, et al. “Materials for Additive Manufacturing.” CIRP Annals, vol. 66, no. 2, Jan. 2017, pp. 659–81. ScienceDirect, doi:10.1016/j.cirp.2017.05.009.

17. Ding, Donghong, et al. “Wire-Feed Additive Manufacturing of Metal Components: Technologies, Developments and Future Interests.” The International Journal of Advanced Manufacturing Technology, vol. 81, no. 1–4, Oct. 2015, pp. 465–81. Crossref, doi:10.1007/s00170-015-7077-3.

18. Mueller, Bernhard, and Detlef Kochan. “Laminated Object Manufacturing for Rapid Tooling and Patternmaking in Foundry Industry.” Computers in Industry, vol. 39, no. 1, June 1999, pp. 47–53. Crossref, doi:10.1016/S0166-3615(98)00127-4.

19. Miyanaji, Hadi, et al. “Process Development of Porcelain Ceramic Material with Binder Jetting Process for Dental Applications.” JOM, vol. 68, no. 3, Mar. 2016, pp. 831–41. Crossref, doi:10.1007/s11837-015-1771-3.

20. Levy, Asaf, et al. “Additive Manufacturing of Complex-Shaped Graded TiC/Steel Composites.” *Materials & Design*, vol. 118, Mar. 2017, pp. 198–203. *ScienceDirect*, doi:10.1016/j.matdes.2017.01.024.

21. Mueller, Bernhard. “Additive Manufacturing Technologies – Rapid Prototyping to Direct Digital Manufacturing.” *Assembly Automation*, vol. 32, no. 2, Apr. 2012. *Crossref*, doi:10.1108/aa.2012.03332baa.010.

22. Carroll, Beth E., et al. “Functionally Graded Material of 304L Stainless Steel and Inconel 625 Fabricated by Directed Energy Deposition: Characterization and Thermodynamic Modeling.” Acta Materialia, vol. 108, Apr. 2016, pp. 46–54. Crossref, doi:10.1016/j.actamat.2016.02.019.

23. Costa, L., et al. “Rapid Tooling by Laser Powder Deposition: Process Simulation Using Finite Element Analysis.” Acta Materialia, vol. 53, no. 14, Aug. 2005, pp. 3987–99. Crossref, doi:10.1016/j.actamat.2005.05.003.

24. Kruth, J. P., et al. “Selective Laser Melting of Iron-Based Powder.” Journal of Materials Processing Technology, vol. 149, no. 1, June 2004, pp. 616–22. ScienceDirect, doi:10.1016/j.jmatprotec.2003.11.051.

25. Frazier, William E. “Metal Additive Manufacturing: A Review.” *Journal of Materials Engineering and Performance*, vol. 23, no. 6, June 2014, pp. 1917–28. *Crossref*, doi:10.1007/s11665-014-0958-z.

26. Thompson, Mary Kathryn, et al. “Design for Additive Manufacturing: Trends, Opportunities, Considerations, and Constraints.” *CIRP Annals*, vol. 65, no. 2, 2016, pp. 737–60. *Crossref*, doi:10.1016/j.cirp.2016.05.004.

27. Lee, Jian-Yuan, et al. “Fundamentals and Applications of 3D Printing for Novel Materials.” *Applied Materials Today*, vol. 7, June 2017, pp. 120–33. *Crossref*, doi:10.1016/j.apmt.2017.02.004.

28. Schniepp, Tim. *ADDITIVE MANUFACTURING FOR COMPOSITE TOOLING*. p. 37. Stratasys Webinar (2017)

29. Pollack, H. W. (1973). *Materials Science and Metallurgy*. Reston, VA: Reston Publishing Company.

30. Wachtman, John B., et al. *Mechanical Properties of Ceramics*. John Wiley & Sons, 2009.

31. Bansal, Narottam P., and Robert H. Doremus. *Handbook of Glass Properties*. Elsevier, 2013.

32. Wan, Wei, et al. "Effect of Sintering Temperature on the Properties of Fused Silica Ceramics Prepared by Gelcasting." *Journal of Electronic Materials*, vol. 43, no. 7, July 2014, pp. 2566–72. *Crossref*, doi:10.1007/s11664-014-3112-7.

33. Jo, Hyu Sang, and Gyo Woo Lee. *Thermal Expansion Coefficient and Young's Modulus of Silica-Reinforced Epoxy Composite*. Vol. 8, no. 11, 2014, p. 4.

34. Shangguan, Haolong, et al. "3D-Printed Shell-Truss Sand Mold for Aluminum Castings." *Journal of Materials Processing Technology*, vol. 250, Dec. 2017, pp. 247–53. *Crossref*, doi:10.1016/j.jmatprotec.2017.05.010.

35. Snelling, Dean, et al. "Lightweight Metal Cellular Structures Fabricated via 3D Printing of Sand Cast Molds." *Advanced Engineering Materials*, vol. 17, no. 7, pp. 923–32. *Wiley Online Library*, doi:10.1002/adem.201400524.

36. Partyka, J., et al. "Effects of Quartz Grain Size Distribution on the Structure of Porcelain Glaze." *Ceramics International*, vol. 40, no. 8, Sept. 2014, pp. 12045–53. *Crossref*, doi:10.1016/j.ceramint.2014.04.044.

37. Keen, David A., and Martin T. Dove. “Local Structures of Amorphous and Crystalline Phases of Silica, SiO_2, by Neutron Total Scattering.” *Journal of Physics: Condensed Matter*, vol. 11, no. 47, Nov. 1999, pp. 9263–73. *Crossref*, doi:10.1088/0953-8984/11/47/311.

38. Swamy, V., et al. “A Thermodynamic Assessment of Silica Phase Diagram.” *Journal of Geophysical Research: Solid Earth*, vol. 99, no. B6, Sept. 2012, pp. 11787–94. *agupubs.onlinelibrary.wiley.com*, doi:10.1029/93JB02968.

39. Koike, C., et al. “INFRARED SPECTRA OF SILICA POLYMORPHS AND THE CONDITIONS OF THEIR FORMATION.” *The Astrophysical Journal*, vol. 778, no. 1, Nov. 2013, p. 60. *Crossref*, doi:10.1088/0004-637X/778/1/60.

40. Kazemi, A., et al. “Investigation on Cristobalite Crystallization in Silica-Based Ceramic Cores for Investment Casting.” *Journal of the European Ceramic Society*, vol. 33, no. 15, Dec. 2013, pp. 3397–402. *ScienceDirect*, doi:10.1016/j.jeurceramsoc.2013.06.025.

41. Breneman, Ryan C., and John W. Halloran. “Effect of Cristobalite on the Strength of Sintered Fused Silica Above and Below the Cristobalite Transformation.” *Journal of the American Ceramic Society*, vol. 98, no. 5, pp. 1611–17. *Wiley Online Library*, doi:10.1111/jace.13505.

42. *Phase Analysis in Zirconia Systems - GARVIE - 1972 - Journal of the American Ceramic Society - Wiley Online Library*. https://onlinelibrary.wiley.com/doi/abs/10.1111/j.1151-2916.1972.tb11290.x. Accessed 9 July 2018

43. *Wieland Zeno™ Zr Disc Zirconium Oxide*. http://www.matweb.com/search/DataSheet.aspx?MatGUID=d245cf5bf6dd420f94f11a976773f3d7&ckck=1. Accessed 23 Oct. 2018.

44. Enochs, Taylor, et al. "Cuspal Flexure of Composite-Restored Typodont Teeth and Correlation with Polymerization Shrinkage Values." *Dental Materials*, vol. 34, no. 1, Jan. 2018, pp. 152–60. *Crossref*, doi:10.1016/j.dental.2017.09.019.

45. Roualdes, Olivier, et al. "In Vitro and in Vivo Evaluation of an Alumina–Zirconia Composite for Arthroplasty Applications." *Biomaterials*, vol. 31, no. 8, Mar. 2010, pp. 2043–54. *Crossref*, doi:10.1016/j.biomaterials.2009.11.107.

46. Özkurt, Zeynep, and Ender Kazazoğlu. "Zirconia Dental Implants: A Literature Review." *Journal of Oral Implantology*, vol. 37, no. 3, June 2011, pp. 367–76. *Crossref*, doi:10.1563/AAID-JOI-D-09-00079.

47. Schneider, H., et al. "Structure and Properties of Mullite—A Review." *Journal of the European Ceramic Society*, vol. 28, no. 2, Jan. 2008, pp. 329–44. *Crossref*, doi:10.1016/j.jeurceramsoc.2007.03.017.

48. Rendtorff, N. M., et al. "Zirconia Toughening of Mullite–Zirconia–Zircon Composites Obtained by Direct Sintering." *Ceramics International*, vol. 36, no. 2, Mar. 2010, pp. 781–88. *Crossref*, doi:10.1016/j.ceramint.2009.11.010.

49. Li, Xiao Chun, et al. "Mechanical and Thermal Expansion Behavior of Laser Deposited Metal Matrix Composites of Invar and TiC." Materials Science and Engineering: A, vol. 282, no. 1–2, Apr. 2000, pp. 86–90. Crossref, doi:10.1016/S0921-5093(99)00781-9.

50. Matsui, Masaaki, and Sōshin Chikazumi. “Analysis of Anomalous Thermal Expansion Coefficient of Fe–Ni Invar Alloys.” *Journal of the Physical Society of Japan*, vol. 45, no. 2, Aug. 1978, pp. 458–65, doi:10.1143/JPSJ.45.458.

51. G K White. “Thermal Expansion of Magnetic Metals at Low Temperatures.” *Proceedings of the Physical Society*, vol. 86, no. 1, 1965, p. 159.

52. M Blackman. “On The Lattice Theory of Expansion.” *Proceedings of the Physical Society*, vol. 74, no. 1, 1959, p. 17.

53. Sumiyama, K., et al. “Characteristic Magnetovolume Effects in Invar Type Fe-Pt Alloys.” *Journal of Physics F: Metal Physics*, vol. 9, no. 8, Aug. 1979, pp. 1665–77. *Crossref*, doi:10.1088/0305-4608/9/8/017.

54. Rancourt, D. G., and M. Z. Dang. “Relation between Anomalous Magnetovolume Behavior and Magnetic Frustration in Invar Alloys.” *Physical Review B*, vol. 54, no. 17, Nov. 1996, pp. 12225–31.

55. Jasthi, Bharat K., et al. “Thermal Expansion Coefficient and Mechanical Properties of Friction Stir Welded Invar (Fe-36%Ni).” *Journal of Materials Engineering and Performance*, vol. 18, no. 7, Oct. 2009, pp. 925–34. *Crossref*, doi:10.1007/s11665-008-9320-7.

56. Vinogradov, A., et al. “Enhanced Strength and Fatigue Life of Ultra-Fine Grain Fe–36Ni Invar Alloy.” *Materials Science and Engineering: A*, vol. 355, no. 1–2, Aug. 2003, pp. 277–85. *Crossref*, doi:10.1016/S0921-5093(03)00082-0.

57. Abberger, Advanced Composite Molds—A New Use for Invar, *The Invar Effect: A Centennial Symposium*, J. Wittenauer, Ed., 7-8 Oct 1996 (Cincinnati, OH), The

Minerals, Metals & Materials Society, 1997, p 317-325Pattnaik, Sarojrani, et al. "Developments in Investment Casting Process—A Review."

58. Pattnaik, Sarojrani, et al. "Developments in Investment Casting Process—A Review." *Journal of Materials Processing Technology*, vol. 212, no. 11, Nov. 2012, pp. 2332–48. *Crossref*, doi:10.1016/j.jmatprotec.2012.06.003.
59. Stachovec, I., et al. "Gating Systems for Sizeable Castings from Al Alloys Cast into Ceramic Moulds." *Archives of Foundry Engineering*, vol. 12, no. 2, Jan. 2012. *Crossref*, doi:10.2478/v10266-012-0038-5.
60. McQueen, H. J., and J. J. Jonas. "Role of the Dynamic and Static Softening Mechanisms in Multistage Hot Working." *Journal of Applied Metalworking*, vol. 3, no. 4, Jan. 1985, pp. 410–20. *Crossref*, doi:10.1007/BF02833663.
61. Sakai, Taku, et al. "Dynamic and Post-Dynamic Recrystallization under Hot, Cold and Severe Plastic Deformation Conditions." *Progress in Materials Science*, vol. 60, Mar. 2014, pp. 130–207. *Crossref*, doi:10.1016/j.pmatsci.2013.09.002.
62. Jahazi, M., and B. Eghbali. "The In¯uence of Hot Forging Conditions on the Microstructure and Mechanical Properties of Two Microalloyed Steels." *Journal of Materials Processing Technology*, 2001, p. 5.
63. Barrau, O., et al. "Analysis of the Friction and Wear Behaviour of Hot Work Tool Steel for Forging." *Wear*, vol. 255, no. 7–12, Aug. 2003, pp. 1444–54. *Crossref*, doi:10.1016/S0043-1648(03)00280-1.
64. Davim, J. Paulo. *Machining: Fundamentals and Recent Advances*. Springer Science & Business Media, 2008.

65. *Nglos324 - Slipcasting*. https://www.princeton.edu/~maelabs/mae324/glos324/slipcasting.htm. Accessed 21 Aug. 2018.

66. Younesi, M., and M. E. Bahrololoom. "Effect of Temperature and Pressure of Hot Pressing on the Mechanical Properties of PP–HA Bio-Composites." *Materials & Design*, vol. 30, no. 9, Oct. 2009, pp. 3482–88. *Crossref*, doi:10.1016/j.matdes.2009.03.011.

67. "The 7 Categories of Additive Manufacturing." *The 7 Categories of Additive Manufacturing | Additive Manufacturing Research Group | Loughborough University*, Loughborough University,

68. Wohlers, Terry, and Tim Gornet. *History of Additive Manufacturing*. 2016, p. 38.

69. Dehurtevent, Marion, et al. "Stereolithography: A New Method for Processing Dental Ceramics by Additive Computer-Aided Manufacturing." *Dental Materials*, vol. 33, no. 5, May 2017, pp. 477–85. *Crossref*, doi:10.1016/j.dental.2017.01.018.

70. Yunus, Doruk Erdem, et al. "Short Fiber Reinforced 3d Printed Ceramic Composite with Shear Induced Alignment." *Ceramics International*, vol. 43, no. 15, Oct. 2017, pp. 11766–72. *Crossref*, doi:10.1016/j.ceramint.2017.06.012.

71. Kang, Jin-wu, and Qiang-xian Ma. "The Role and Impact of 3D Printing Technologies in Casting." *China Foundry*, vol. 14, no. 3, May 2017, pp. 157–68. *Crossref*, doi:10.1007/s41230-017-6109-z.

72. Baumers, M., et al. *HOW CAN MATERIAL JETTING SYSTEMS BE UPGRADED FOR MORE EFFICIENT MULTI-MATERIAL ADDITIVE MANUFACTURING?* p. 15.

73. Bai, Yun, and Christopher B. Williams. "Binder Jetting Additive Manufacturing with a Particle-Free Metal Ink as a Binder Precursor." *Materials & Design*, vol. 147, June 2018, pp. 146–56. *Crossref*, doi:10.1016/j.matdes.2018.03.027.

74. Hwang, Seyeon, et al. "Thermo-Mechanical Characterization of Metal/Polymer Composite Filaments and Printing Parameter Study for Fused Deposition Modeling in the 3D Printing Process." *Journal of Electronic Materials*, vol. 44, no. 3, Mar. 2015, pp. 771–77. *Crossref*, doi:10.1007/s11664-014-3425-6.

75. Tian, Xiaoyong, et al. "Interface and Performance of 3D Printed Continuous Carbon Fiber Reinforced PLA Composites." *Composites Part A: Applied Science and Manufacturing*, vol. 88, Sept. 2016, pp. 198–205. *Crossref*, doi:10.1016/j.compositesa.2016.05.032.

76. Matsuzaki, Ryosuke, et al. "Three-Dimensional Printing of Continuous-Fiber Composites by in-Nozzle Impregnation." *Scientific Reports*, vol. 6, no. 1, Sept. 2016. *Crossref*, doi:10.1038/srep23058.

77. Campbell, Ian, et al. "Additive Manufacturing: Rapid Prototyping Comes of Age." *Rapid Prototyping Journal*, vol. 18, no. 4, June 2012, pp. 255–58. *Crossref*, doi:10.1108/13552541211231563.

78. Irrinki, Harish, et al. "Effects of Powder Attributes and Laser Powder Bed Fusion (L-PBF) Process Conditions on the Densification and Mechanical Properties of

17-4 PH Stainless Steel." *JOM*, vol. 68, no. 3, Mar. 2016, pp. 860–68. *Crossref*, doi:10.1007/s11837-015-1770-4.

79. Rashid, R., et al. "Effect of Scan Strategy on Density and Metallurgical Properties of 17-4PH Parts Printed by Selective Laser Melting (SLM)." *Journal of Materials Processing Technology*, vol. 249, Nov. 2017, pp. 502–11. *Crossref*, doi:10.1016/j.jmatprotec.2017.06.023.
80. Gibson, I., et al. *Additive Manufacturing Technologies: 3D Printing, Rapid Prototyping and Direct Digital Manufacturing*. Second edition, Springer, 2015.
81. Bournias-Varotsis, Alkaios, et al. "Ultrasonic Additive Manufacturing as a Form-Then-Bond Process for Embedding Electronic Circuitry into a Metal Matrix." *Journal of Manufacturing Processes*, vol. 32, Apr. 2018, pp. 664–75. *Crossref*, doi:10.1016/j.jmapro.2018.03.027.
82. Kakinuma, Yasuhiro, et al. "Influence of Metal Powder Characteristics on Product Quality with Directed Energy Deposition of Inconel 625." *CIRP Annals*, vol. 65, no. 1, 2016, pp. 209–12. *Crossref*, doi:10.1016/j.cirp.2016.04.058.
83. Denlinger, Erik R., et al. "Effect of Inter-Layer Dwell Time on Distortion and Residual Stress in Additive Manufacturing of Titanium and Nickel Alloys." *Journal of Materials Processing Technology*, vol. 215, Jan. 2015, pp. 123–31. *Crossref*, doi:10.1016/j.jmatprotec.2014.07.030.
84. Dinda, G. P., et al. "Laser Aided Direct Metal Deposition of Inconel 625 Superalloy: Microstructural Evolution and Thermal Stability." *Materials Science*

and Engineering: A, vol. 509, no. 1–2, May 2009, pp. 98–104. *Crossref*, doi:10.1016/j.msea.2009.01.009.

85. Jendrzejewski, Rafał, and Gerard Śliwiński. "Investigation of Temperature and Stress Fields in Laser Cladded Coatings." *Applied Surface Science*, vol. 254, no. 4, Dec. 2007, pp. 921–25. *Crossref*, doi:10.1016/j.apsusc.2007.08.014.
86. Heigel, J. C., et al. "Thermo-Mechanical Model Development and Validation of Directed Energy Deposition Additive Manufacturing of Ti–6Al–4V." *Additive Manufacturing*, vol. 5, Jan. 2015, pp. 9–19. *Crossref*, doi:10.1016/j.addma.2014.10.003.
87. Hofmann, Douglas C., et al. "Developing Gradient Metal Alloys through Radial Deposition Additive Manufacturing." *Scientific Reports*, vol. 4, no. 1, May 2015. *Crossref*, doi:10.1038/srep05357.
88. Bobbio, Lourdes D., et al. "Additive Manufacturing of a Functionally Graded Material from Ti-6Al-4V to Invar: Experimental Characterization and Thermodynamic Calculations." *Acta Materialia*, vol. 127, Apr. 2017, pp. 133–42. *Crossref*, doi:10.1016/j.actamat.2016.12.070.
89. Maleksaeedi, S., et al. "Property Enhancement of 3D-Printed Alumina Ceramics Using Vacuum Infiltration." *Journal of Materials Processing Technology*, vol.
90. Gonzalez, J. A., et al. "Characterization of Ceramic Components Fabricated Using Binder Jetting Additive Manufacturing Technology." *Ceramics International*, vol. 42, no. 9, July 2016, pp. 10559–64. *Crossref*, doi:10.1016/j.ceramint.2016.03.079.

91. Myers, Kyle. *Structure-Property Relationship of Binder Jetted Fused Silica Preforms to Manufacture Ceramic-Metallic Interpenetrating Phase Composites*. p. 252.

92. Agarwal, Bhagwan D., et al. *Analysis and Performance of Fiber Composites*. John Wiley & Sons, 2017.

93. Naslain, R. "Design, Preparation and Properties of Non-Oxide CMCs for Application in Engines and Nuclear Reactors: An Overview." *Composites Science and Technology*, vol. 64, no. 2, Feb. 2004, pp. 155–70. *Crossref*, doi:10.1016/S0266-3538(03)00230-6.

94. Zok, Frank W. "Ceramic-Matrix Composites Enable Revolutionary Gains in Turbine Engine Efficiency." *American Ceramic Society Bulletin*, vol. 95, no. 5, p. 7.

95. Zhu, Wei, et al. "Fabrication and Characterization of Carbon Fiber Reinforced SiC Ceramic Matrix Composites Based on 3D Printing Technology." *Journal of the European Ceramic Society*, vol. 38, no. 14, Nov. 2018, pp. 4604–13. *Crossref*, doi:10.1016/j.jeurceramsoc.2018.06.022.

96. Stewart, Todd D., et al. "Long-Term Wear of Ceramic Matrix Composite Materials for Hip Prostheses under Severe Swing Phase Microseparation." *Journal of Biomedical Materials Research*, vol. 66B, no. 2, Aug. 2003, pp. 567–73. *Crossref*, doi:10.1002/jbm.b.10035.

97. Jayalekshmi, A. C., and Chandra P. Sharma. "Gold Nanoparticle Incorporated Polymer/Bioactive Glass Composite for Controlled Drug Delivery Application."

Colloids and Surfaces B: Biointerfaces, vol. 126, Feb. 2015, pp. 280–87. *Crossref*, doi:10.1016/j.colsurfb.2014.12.021.

98. Affatato, Saverio, et al. "Advanced Biomaterials in Hip Joint Arthroplasty. A Review on Polymer and Ceramics Composites as Alternative Bearings." *Composites Part B: Engineering*, vol. 83, Dec. 2015, pp. 276–83. *Crossref*, doi:10.1016/j.compositesb.2015.07.019.
99. Bhatt, Alpa Tapan, et al. "Primary Manufacturing Processes for Fiber Reinforced Composites: History, Development & Future Research Trends." *IOP Conference Series: Materials Science and Engineering*, vol. 330, Mar. 2018, p. 012107. *Crossref*, doi:10.1088/1757-899X/330/1/012107.
100. Sciti, D., et al. "From Random Chopped to Oriented Continuous SiC Fibers–ZrB2 Composites." *Materials & Design*, vol. 63, Nov. 2014, pp. 464–70. *Crossref*, doi:10.1016/j.matdes.2014.06.037.
101. Dickson, Andrew N., et al. "Fabrication of Continuous Carbon, Glass and Kevlar Fibre Reinforced Polymer Composites Using Additive Manufacturing." *Additive Manufacturing*, vol. 16, Aug. 2017, pp. 146–52. *Crossref*, doi:10.1016/j.addma.2017.06.004.
102. Fu, Shao-Yun, et al. "Effects of Particle Size, Particle/Matrix Interface Adhesion and Particle Loading on Mechanical Properties of Particulate–Polymer Composites." *Composites Part B: Engineering*, vol. 39, no. 6, Sept. 2008, pp. 933–61. *Crossref*, doi:10.1016/j.compositesb.2008.01.002.

103. Elmer, J. Vv, et al. *The Thermal Expansion Characteristics of Stainless Steel Weld Metal*. p. 9.

104. Boothroyd, Geoffrey. *Fundamentals of Metal Machining and Machine Tools, Third Edition*. CRC Press, 1988.

105. Fischer, Fred. "THERMOPLASTICS: THE BEST CHOICE FOR 3D PRINTING." *D Printing*, p. 5.

106. A.A. Hassen, J. Lindahl, X. Chen, B. Post, L. Love, V. Kunc. "Additive manufacturing of composite tooling using high temperature thermoplastic materials." SAMPE Conference Proceedings, Long Beach, CA, May 23-26 (2016), pp. 2648-2658

107. Kunc, Vlastimil, et al. *INVESTIGATION OF IN-AUTOCLAVE ADDITIVE MANUFACTURING COMPOSITE TOOLING*. p. 10.

108. Ding, Donghong, et al. "Wire-Feed Additive Manufacturing of Metal Components: Technologies, Developments and Future Interests." *The International Journal of Advanced Manufacturing Technology*, vol. 81, no. 1–4, Oct. 2015, pp. 465–81. *Crossref*, doi:10.1007/s00170-015-7077-3.

109. Jason B. Jones. *Repurposing Mainstream CNC Machine Tools for Laser-Based Additive Manufacturing*. Vol. 9738, 2016, pp. 973811-9738–11, https://doi.org/10.1117/12.2217901.

110. Soutis, C. "Carbon Fiber Reinforced Plastics in Aircraft Construction." *Materials Science and Engineering: A*, vol. 412, no. 1–2, Dec. 2005, pp. 171–76. *Crossref*, doi:10.1016/j.msea.2005.08.064.

111. Sadeghian, Ramin, et al. “Manufacturing Carbon Nanofibers Toughened Polyester/Glass Fiber Composites Using Vacuum Assisted Resin Transfer Molding for Enhancing the Mode-I Delamination Resistance.” *Composites Part A: Applied Science and Manufacturing*, vol. 37, no. 10, Oct. 2006, pp. 1787–95. *Crossref*, doi:10.1016/j.compositesa.2005.09.010.

112. Hammami, A., and B. R. Gebart. “Analysis of the Vacuum Infusion Molding Process.” *Polymer Composites*, vol. 21, no. 1, Feb. 2000, pp. 28–40. *Crossref*, doi:10.1002/pc.10162.

113. Mazumdar, Sanjay. *Composites Manufacturing: Materials, Product, and Process Engineering*. CRC Press, 2001. *Crossref*, doi:10.1201/9781420041989.

114. Sadeghian, Ramin, et al. “Manufacturing Carbon Nanofibers Toughened Polyester/Glass Fiber Composites Using Vacuum Assisted Resin Transfer Molding for Enhancing the Mode-I Delamination Resistance.” *Composites Part A: Applied Science and Manufacturing*, vol. 37, no. 10, Oct. 2006, pp. 1787–95. *Crossref*, doi:10.1016/j.compositesa.2005.09.010.

115. Fette, M., et al. “Automated and Cost-Efficient Production of Hybrid Sheet Moulding Compound Aircraft Components.” *Procedia Manufacturing*, vol. 6, 2016, pp. 132–39. *Crossref*, doi:10.1016/j.promfg.2016.11.017.

116. Zhao, Huoping, et al. *3D Printing of ZrO2 Ceramic Using Nano-Zirconia Suspension as a Binder*. Atlantis Press, 2016. *Crossref*, doi:10.2991/icsmim-15.2016.122.

117. Leamy, H. J., et al. “Plastic Flow and Fracture of Metallic Glass.” *Metallurgical and Materials Transactions B*, vol. 3, no. 3, Mar. 1972. *Crossref*, doi:10.1007/BF02642754.

118. Boey, F. Y. C., and S. W. Lye. “Void Reduction in Autoclave Processing of Thermoset Composites: Part 1: High Pressure Effects on Void Reduction.” *Composites*, vol. 23, no. 4, July 1992, pp. 261–65, doi:10.1016/0010-4361(92)90186-X.

119. D. Snelling, H. Blount, C. Forman, K. Ramsburg, A. Wentzel, C. Williams, et al.The effects of 3D pritned molds on metal castings
Solid Free Fabr Symp (2013), pp. 827-845

120. Private conversations with Steve Szaruga from the Multi-Scale Composites & Polymer Division. UDRI. Dayton, OH.

121. Angelastro, A., et al. “Statistical Analysis and Optimization of Direct Metal Laser Deposition of 227-F Colmonoy Nickel Alloy.” *Optics & Laser Technology*, vol. 94, Sept. 2017, pp. 138–45. *Crossref*, doi:10.1016/j.optlastec.2017.03.027.